MOVING-MESH HYDRODYNAMIC SIMULATIONS OF COLLIDING WIND BINARIES

James R. Good
Advisor: Assoc. Prof. Shazrene Mohamed

Submitted in partial completion of the
BS in Astronomy-Physics Major

Department of Astronomy
University of Virginia
Charlottesville, VA, United States

May 14, 2025

ABSTRACT

While theories for stellar evolution are well developed for single stars, the majority of massive stars are found in binary systems, which gives rise to different evolutionary pathways, phenomena and fates for these stars. Colliding wind binaries, systems in which both massive stars have strong stellar winds, are ideal laboratories for exploring the complex hydrodynamics in wind interacting regions, given the extensive and detailed multi-wavelength studies from X-rays to radio of the high and low energy emission produced by processes such as particle acceleration and dust formation. High resolution, multi-dimensional simulations of colliding wind binaries can provide insight towards the specific mass configurations, instabilities, and hydrodynamics of these complicated shocked wind colliding regions. In this paper, we begin with a description of the observations and physics of stellar winds, in particular the line-driven winds that characterize the stars in colliding wind binaries. We then present hydrodynamic simulations of stellar winds and colliding wind binaries using the moving-mesh magnetohydrodynamics simulation code AREPO to generate predictions for single and binary systems with immense stellar winds. We demonstrate that the two and three-dimensional AREPO simulations of a stellar outflow from a single star are in good agreement with analytical solutions for a spherically symmetric, stationary stellar wind. Having established that the code captures the relevant physics for a single stellar outflow, we apply the same numerical methods to colliding wind binaries. Our colliding wind binary simulations are able to achieve an accurate contact discontinuity location to within 1.9% of the analytical solution, an adiabatic strong-shocked density, temperature and velocity, accurate to within 2%, 8.6% and 34%, respectively, and an isothermal shocked density accurate to within 22%. Modeling these colliding wind binary systems is challenging due to the large dynamical range in fluid properties required to resolve shocks and instabilities while maintaining well-defined boundaries of the stars. While this has been previously explored with adaptive mesh refinement and smooth particle hydrodynamics studies, applying AREPO's unique moving-mesh numerical methods to colliding wind binaries lays the groundwork for future, complementary modeling, including detailed radiative cooling, shock stability, dust formation, X-ray and radio emission, and binary evolution.

1. INTRODUCTION

Early type massive stars produce powerful, dense and high-velocity stellar winds before ending their lives as energetic, core-collapse supernova explosions. The mass-loss through stellar winds not only impacts the pre-supernova stellar evolution of massive stars, but also the properties and characteristics of the supernovae they produce. Analysis of core-collapse supernova observations, particularly at radio wavelengths, indicate large amounts of circumstellar material (CSM) surrounding Type II (exhibit H-lines in their spectra) and Type Ib/c (stripped supernovae that have H-poor spectra) supernovae, many of which can be explained with density profiles falling off as r^{-2} – as expected for constant velocity, steady stellar winds. However, there are an increasing number of systems that require extreme mass-loss rates or show evidence for strong variations or oscillations in their light curves, e.g., SN 1988Z or SN 1979C (Panagia & Bono (2000), Smith (2017)). Since a the majority of massive stars are found in a binary system, (Sana et al. 2012), binary wind interactions could greatly affect the CSM surrounding a large fraction of supernovae progenitors. A deeper understanding of the stellar evolutionary processes in massive stars alongside stellar wind theory and a computational prediction of colliding wind binary structures could allow for more accurate predictions of progenitor objects when analyzing supernovae or supernovae remnants. We hope that the simulations and discussions here will contribute to advancing our understanding of the binary system progenitors that must be studied in order to explain supernovae observations.

First, we broadly cover stellar evolutionary theory, with a particular emphasis on Wolf-Rayet stars and the issues with their origin and evolution. Then, Section 3 covers theories for mass loss via stellar winds, including analytical solutions for stationary, spherically symmetric stellar winds, the physical processes behind line driven stellar winds, and some observational properties of stars with large outflows. Section 4 begins to discuss how the known theories of stellar evolution and winds are complicated in binary systems, and provides justification for why colliding wind binaries demand further analysis. We cover wind interaction physics and establish analytical metrics to test the CWB simulations. We then cover the numerical methods in the AREPO code in Section 5, including discretization techniques, the moving mesh, and the numerical hydrodynamics. Finally, we present our results for both single star and CWB simulations, and discuss our techniques for analyzing the simulations. We conclude in Section 7 with an outline of our plans for improvements and future work.

2. STELLAR EVOLUTION

For high mass stars with $M \gtrsim 15\ M_\odot$, mass loss due to intense stellar winds has an increasingly critical effect on the evolutionary process as the timescale for mass loss due to winds approaches the timescale for evolution due to nuclear fusion (Pols 2011). de Jager et al. (1988) derived an empirical model for predicting the mass-loss rate ($-\dot{M}$) based on the effective temperature ($T_{\rm eff}$) and luminosity (L) of a star:

$$\log(-\dot{M}) \approx -8.16 + 1.77 \log\left(\frac{L}{L_\odot}\right) - 1.68 \log(T_{\rm eff})\,. \tag{1}$$

Combining this equation with observational results from a Hertzsprung-Russell diagram allows for loose predictions of how the mass-loss rate changes with a star's evolving temperature and luminosity, (see Section 3 for an outline of stellar wind theory and wind driving mechanisms). The most luminous stars near the Humphreys-Davidson limit are observed to undergo periods of intense mass loss and experience large fluctuations in both temperature and luminosity. This limit can be understood following Rybicki & Lightman (1985); a spherically symmetric object surrounded by an optically thin cloud with frequency independent absorption coefficient κ, experiences a radiative force per unit mass of

$$f_{\rm rad} = \frac{\kappa L}{4\pi r^2 c}\,, \tag{2}$$

where r is the radial distance from the star, and c is the speed of light. Equating this outward radiative force to the inward gravitational force of the star of mass M leads to the upper luminosity limit for stars in which material is *not* ejected from the star:

$$f_{\rm G} = \frac{GM}{r^2} \to f_{\rm rad} = f_{\rm G} \to L = \frac{4\pi c GM}{\kappa}\,, \tag{3}$$

where G is the gravitational constant. For ionized hydrogen, the absorption coefficient becomes $\kappa = \sigma_T/m_H$, (where σ_T is the Thompson scattering cross-section for the electron and m_H is the mass of H), leading to the accepted expression for a star's Eddington luminosity, $L_{\rm edd}$,:

$$L_{\rm edd} = \frac{4\pi GMcm_H}{\sigma_T} = 3.2\times10^4\left(\frac{M}{M_\odot}\right) L_\odot\,. \tag{4}$$

This is the maximum luminosity of a star that has no outflow of material. This limit corresponds to a red supergiant upper mass limit of $40 M_\odot$, and is theorized as one of the driving physical properties of the Humphrey-Davidson limit on the Hertzsprung-Russell diagram (Pols 2011).

It is thought (see e.g., (Pols 2011) and the references therein) that the luminous blue variable (LBV) stars with mass-loss rates up to $\dot{M} \gtrsim 10^{-3} M_\odot\ {\rm yr}^{-1}$ can eventually lose their outer layers and become Wolf-Rayet (WR) stars. WR stars themselves exhibit massive stellar winds, and are often observed in colliding wind binary (CWB) systems. As such, these systems may hold important clues to understanding extreme mass loss, and their formation and evolution deserves attention.

2.1. *Wolf-Rayet Stars*

WR stars, first discovered by Charles J.E. Wolf and Georges-Antoine-Pons Rayet in 1867, are massive stars characterized by broad, strong emission lines of heavy elements and extremely high surface temperatures. As depicted by the optical spectrum of WR 137 in Figure 1, the strong emission lines corresponding to C, N and O indicate depleted H and an exposed nuclear-fusing core (Pols 2011). WR sub-classifications depend on the relative abundances of heavy surface elements: stars with strong N and He abundances with H are classified as WNL, while WNE stars have similar

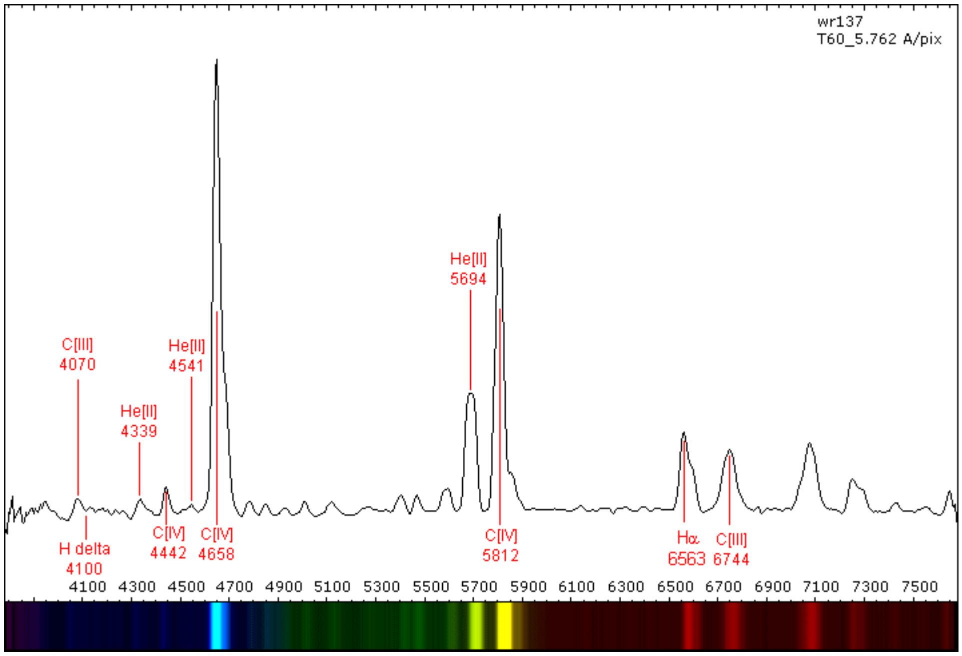

Figure 1. Optical spectrum of WR 137, a WC7 star showing evidence of H depletion with relatively weak H lines compared to the strong emission lines of heavy elements. Image Credit: Gypaete.

N and He abundances but depleted H. Stars with strong C, O and He abundances with little N and almost no H are WC stars, while WO stars have even higher O abundances (Smith 1968). Crowther (2007) and other suggest that the sub-classification of WR stars follows an "early" to "late" evolutionary sequence, in which WNL stars are H-fusing, WC stars are partially He-fusing and WO stars are completely He-fusing.

The depletion of H in WC and "later" WR stars leads to incredibly high luminosities, greatly exceeding the theoretical "maximum" luminosity described in Equation 4. As such, WR stars have extremely strong and dense stellar winds. The extensive mass loss WR stars experience makes their evolutionary sequences difficult to identify. Abbott & Conti (1987) were the first to suggest that WR stars evolve from O stars undergoing extreme mass loss due to strong stellar winds, stripping the outermost layers and revealing the core, (known as the "Conti scenario"). However, the observed association of WR stars as LBV phase objects complicated this generic evolutionary sequence. An alternative consideration is WR evolution resulting from H envelope stripping due to binary interaction (Crowther 2007).

While WR stars demand attention due to their role as both supernova and Gamma-Ray Burst (GRB) progenitors, they are also interesting in the case of colliding wind binaries, where WR stars are likely to be an important source of dust in the interstellar medium (ISM) (Lau et al. 2022). Observationally, as discussed by Crowther (2007) and the references therein, the photo-ionized material ejected from WR stars forms extended nebulae in the ISM. The material in these nebulae can yield information about the past life of the WR star and can constrain the evolutionary path taken to reach its current state. The strong stellar winds of WR stars will plow through the previously ejected material from the "slow wind" precursor object. Studies of the "slower" winds of LBV, O, or red supergiant (RSG) stars being shocked and/or swept up by WR winds have been compared with observations of a ring nebula surrounding young WR stars, to gain insight into the evolutionary sequences of stars into the WR phase (van Marle & Keppens 2012).

2.2. *Binary Evolution*

The presence of a stellar companion further complicates the mysteries surrounding WR stars, their evolution, and their role as supernova or GRB progenitors. van der Hucht (2001) estimates that 39% of Galactic WR stars are in a binary system. However, since the majority of WR binary stars have an O or B type companion, it is possible that observed isolated WR stars were formed in a binary and were ejected from the system when their stellar companion underwent a supernova explosion (White & Tuthill 2024). Regardless, the presence of a massive binary companion often affects WR evolutionary sequences. Crowther (2007) suggests that WR stars in binaries could either evolve independently from their stellar companion (expected in wide binaries), or, evolve *with* their stellar companion due to the exchange of mass and momentum. More recent studies indicate that close interacting binary evolution seems to be increasingly important understanding WR and other massive stars (Sana et al. 2012; White & Tuthill 2024).

Close binary evolution drastically affects the evolution of massive stars. Sana et al. (2012) found that 71% of O stars "interact" with a stellar companion, 20 to 30% will result in a binary merger, and 40 to 50% will either accrete significant mass from a stellar companion or be stripped of significant mass. Even more significantly, they suggest that approximately three quarters of *all massive stars* will be strongly affected by some binary interaction before a supernova explosion. These exceptional observational statistics certainly raise more questions than they answer, however. Massive star evolutionary models are inevitably complicated by binary interaction, as the interiors of stars accreting significant material are mixed and envelopes are spun up by a gain in angular momentum (Brott et al. 2011). Furthermore, it seems likely that WR stars form as a result of significant Roche lobe mass stripping due to gravitational interaction with a large stellar companion. Crowther (2007) suggests that WR evolution via such binary interaction, which allows for lower initial mass and luminosity constraints on the WR precursor, is more favorable.

Binary "interaction" is typically characterized by mass transfer between stars in a binary system. Each stellar object has a region in space in which its own gravity is the most dominant, known as the *Roche lobe*. The size of the Roche lobes depends on the ratio of the stellar masses and the orbital separation. Mass transfer, known as Roche-lobe overflow, from one star to the other occurs when a star expands (e.g., becoming a RSG) or the orbit shrinks, such that the outermost edge of the star itself exists at the intersection between the Roche lobes, known as the L1 Lagrange point. Material flows through the L1 point and into the potential well of the accretor. The pool of closely interacting binaries suggest that the majority of the larger, primary stars begin to donate mass to the secondary in the H-shell burning phase or the He-shell burning phase, as opposed to the H-core burning main sequence phase (Crowther 2007). However, mass and angular momentum transfer can also occur via stellar winds (Edgar 2004). Wind accretion onto either star will occur if one of the stars has a strong stellar wind. In the case where both stars have strong winds, the winds will collide, and the resulting structures provide interesting information on the hydrodynamics of stellar wind mechanisms and the evolutionary processes inside the stars (see Section 4).

3. MASS LOSS VIA STELLAR WINDS

Mass loss plays a pivotal role in stellar evolution, impacting a star's life expectancy, evolutionary sequence, and final fate (e.g., strength and type, if any, of supernova explosion). In massive early-type stars where temperatures are too high to allow the formation of dust grains, radiation interacts with material in the outer stellar atmospheres at wavelengths where the outer material is highly opaque, resulting in acceleration due to many ultraviolet lines. *Line driven* radiation theory predicts very high wind speeds due to the continuous transfer of energy and momentum from the ejected radiation at redder and redder photon wavelengths, as the material is accelerated towards terminal velocity (Cassinelli 1979). Doppler broadening of the opaque wind lines results in a "positive feedback mechanism", allowing the wind to continually absorb photons of higher and higher energy and allowing massive acceleration to high velocities (Pols 2011). While line-driven radiation theory is well understood, observed inhomogeneities and asymmetries make realizing predictions difficult. The subject of this work, the shock interaction between two stellar winds in colliding wind binaries (CWBs) and the often luminous, multi-wavelength emission produced, is a useful tool to probe both the hydrodynamic processes of stellar wind mechanisms and the evolutionary phases of the interacting stars. However, we begin with an outline of the analytic and theoretical expectations for idealized, single star winds.

3.1. *Wind from a Single, Spherically Symmetric Star*

Following Gawryszczak et al. (2002), we derive differential equations for the density and velocity of a spherically symmetric, stationary wind. The continuity equation for stellar winds relates the velocity, $v(r)$, and density, $\rho(r)$, distributions as functions of the radial coordinate:

$$\dot{M} = 4\pi r^2 \rho(r) v(r)\,. \tag{5}$$

The momentum conservation equation is

$$v\frac{dv}{dr} = -\frac{1}{\rho}\frac{dP}{dr}\,, \tag{6}$$

where P is the gas pressure, and we disregard the gravitational deceleration, $\frac{GM}{r^2}$, assuming it is exactly balanced by a wind acceleration mechanism (see Section 3.2). Explicit analytical solutions can be simplified using the polytrope equation of state. Chandrasekhar (Chandrasekhar 1939) concluded from the prior work of Kelvin, Lane, and Emden that a quasi-static adiabatic process will have the form

$$P = K\rho^{\gamma}\,, \tag{7}$$

for a constant, K, and where γ, the adiabatic index, pertains to the ratio of the specific heats of the gas and is related to the polytropic index by $\gamma = (n+1)/n$. This famous *polytrope relation* provides a simple, useful, and intuitive model for pressure and density in stars and large self-gravitating objects. Use of the chain rule leads to the pressure radial derivative:

$$\frac{dP}{dr} = \frac{dP}{d\rho}\frac{d\rho}{dr} = K\gamma\rho^{\gamma-1}\frac{d\rho}{dr}\,, \tag{8}$$

which, when substituted into Equation 6 yields:

$$v\frac{dv}{dr} = -K\gamma\rho^{\gamma-2}\frac{d\rho}{dr}\,. \tag{9}$$

Taking the radial derivative of mass continuity (Equation 5) provides us with a 'pivot equation':

$$\frac{d\rho}{dr} = -\frac{\dot{M}}{4\pi}\left(\frac{2}{r^3 v} + \frac{1}{r^2 v^2}\frac{dv}{dr}\right)\,. \tag{10}$$

The set of Equations 9 and 10, in combination with mass continuity (Equation 5) allow us to directly express differential equations for wind density and velocity as a function of radial distance from the star, with constant parameters polytrope proportionality constant, K, adiabatic index, γ, and mass-loss rate, $\dot{M}$, where we substitute the constant $\alpha = \dot{M}/4\pi$, as done in Gawryszczak et al. (2002):

$$\frac{d\rho}{dr} = \frac{\rho}{r}\frac{2}{K\gamma\alpha^{-2}\rho^{\gamma+1}r^4 - 1}\,. \tag{11}$$

$$\frac{dv}{dr} = \frac{v}{r}\frac{2K\gamma}{r^{2\gamma-2}v^{\gamma+1}\alpha^{1-\gamma} - K\gamma}\,. \tag{12}$$

The early 19th century empirical thermodynamic work done by Avogadro, Charles, Boyle, and Gay-Lussac was compiled into the famous *ideal gas law* by Clapeyron (1834). Here, we use the form involving density, average particle mass, μ, and $m_H = 1.67 \times 10^{-24}$ g:

$$P = \frac{\rho k_B T}{\mu m_H}\,. \tag{13}$$

Taking advantage of the polytrope relation again, (Equation 7), we eliminate pressure and express the temperature, T, of the wind as a function of density with constant parameters, γ, and the initial wind temperature and density, T_0 and ρ_0:

$$T = T_0\left(\frac{\rho}{\rho_0}\right)^{\gamma-1}\,. \tag{14}$$

3.2. *Line-driven Winds*

The bulk of the radiation emitted by hot stars is at ultraviolet wavelengths, for which the outer atmosphere has many absorption lines with very high opacity, up to 10^6 times the opacity of electron scattering, (Lamers & Cassinelli 1999). The Doppler shift plays a crucial role in efficient line driving. In a static atmosphere, photons are absorbed and scattered in regions closer to the star's center. When the outer atmosphere is accelerating outwards, increasingly red-shifted photons are able to contribute their momenta to the outermost parts of the atmosphere, allowing for a continuous 'feedback loop' of radiation transfer. Consider an atom moving radially outwards at velocity v_r. After absorbing a photon, the momentum of the atom increases by $mv'_r = mv_r + h\nu/c$, where m is the mass of the atom, ν is its frequency and $h = 6.626 \times 10^{-27}$ erg s^{-1} is the Planck constant, such that the increase in velocity is $\Delta v = h\nu/mc$. Then, the atom emits a photon at a new frequency in a random direction α with respect to the radial trajectory, and the post-emission momentum is $mv_r'' = mv_r' - \frac{h\nu'}{c}\cos\alpha$.

If the atom can only absorb and emit a photon of frequency ν_0 in the rest frame, the observer sees a photon absorbed at $\nu = \nu_0(1+v_r/c)$ and emitted at $\nu' = \nu_0(1+v'_r/c)$. The atom's post-emission velocity can then be written in terms of the initial velocity and the rest frequency:

$$v_r'' = v_r + \frac{h\nu_0}{mc}\left(1+\frac{v_r}{c}\right)(1-\cos\alpha) - \frac{1}{c}\left(\frac{h\nu_0}{mc}\right)^2\left(1+\frac{v_r}{c}\right)\cos\alpha\,.$$

In the non-relativistic limit, when $v_r \ll c$ and $h\nu_0 \ll mc$, $h\nu_0/mc$ is small and higher order terms can be disregarded:

$$\Delta v = v_r'' - v_r \simeq \frac{h\nu_0}{mc}(1-\cos\alpha)\ . \tag{15}$$

This equation implies that there is no net change in momentum during forward scattering, where $\alpha = 0$, and that backward scattering, where $\alpha = \pi$, results in a net change in momentum $\Delta p = 2h\nu_0/c$. During de-excitation photons are emitted in a random direction, so the mean momentum transfer is given by the average value over a sphere:

$$\langle \Delta mv \rangle = \frac{h\nu_0}{c}\frac{1}{4\pi}\int_0^\pi 2\pi(1-\cos\alpha)\sin\alpha\, d\alpha = \frac{h\nu_0}{c}\,.$$

Consequently, the change in the momentum is the same for isotropic resonance scattering and pure absorption. Additionally, in the non-relativistic limit, diffuse isotropic radiation produces zero acceleration (Lamers & Cassinelli 1999).

3.3. *Line-driven Winds: Coulomb Coupling*

To achieve a steady outflow of material, the imparted momentum must be equally distributed among the atoms. Absorbing atoms interact electrically with surrounding elements and distribute the imparted momentum in a process named *coulomb coupling.* The transfer of momentum from an absorbing atom to the surrounding plasma field is efficient if the time to slow down by field interactions, t_s, is small compared to the time to reach a large drift velocity, t_d. That is, the condition for Coulomb Coupling is

$$t_s < t_d\,. \tag{16}$$

For an element with atomic mass A, charge Z, electron number density n_e and a wind temperature T_e, the slow down time in seconds is given by (Spitzer (1962), page 135):

$$t_s = 0.305\frac{A}{Z^2}\frac{{T_e}^{3/2}}{n_e(1-0.022\ \ln\ n_e)}\,. \tag{17}$$

The drift time is the time for incident photons to increase the momentum of an atom by an amount equal to the thermal velocity of the plasma. In terms of the atom's acceleration due to momentum transfer and the thermal velocity, the drift time is

$$t_d = v_{th}/g_i\,, \tag{18}$$

where the thermal velocity, v_{th}, of the field is given by

$$v_{th} = \left(\frac{2k}{m_H}\right)^{1/2}\left(\frac{T_e}{A_f}\right)^{1/2}, \tag{19}$$

and the acceleration of a non-field-interacting atom, g_i, is given by the change in momentum

$$\frac{d(mv)}{dt} = Am_H g_i = \frac{\pi e^2}{m_e c}\frac{\mathscr{F}_{\nu_0}}{c}f\,, \tag{20}$$

where $m = Am_H$ was used, f is the oscillator strength of the transition and $\mathscr{F}_{\nu_0}$ is the energy flux a distance r from the star at line rest frequency ν_0. The flux at the stellar surface is $\mathscr{F}^*_{\nu_0} = L^*_{\nu_0}/4\pi R^2$, so the flux a distance r from the star is related to the flux at the surface by $\mathscr{F}_{\nu_0} = \mathscr{F}^*_{\nu_0}\left(\frac{R}{r}\right)^2$. The coulomb coupling condition given in Equation 16 is satisfied when

$$\frac{L^*_{\nu_0}T_e}{4\pi r^2 n_e} < \frac{Z^2 c}{0.61}\sqrt{2km_H}\left(\frac{\pi e^2}{m_e c}f\right)^{-1}{A_f}^{-1/2}\,. \tag{21}$$

The Planck law describes the spectral density of electromagnetic radiation for a blackbody in thermal equilibrium:

$$B_\nu(\nu, T) = \frac{2h\nu^3}{c^2} \frac{1}{\exp\left(\frac{h\nu}{k_B T}\right) - 1} . \tag{22}$$

If the wind temperature is $T_e \simeq 0.5\ T_{\rm eff}$, the peak of the Planck law occurs at frequency $\nu_{\rm max} = 5.83 \times 10^{10}\ T_{\rm eff}$, leading to a peak flux of $\mathscr{F}_{\nu_{\rm max}} = 5.97 \times 10^{-16}\ T_{\rm eff}^3$. We rewrite the electron number density in terms of the wind density, $n_e = 5.2 \times 10^{23}\ \rho$, and substitute the wind density for constant mass-loss rate, (Equation 5), to express the coupling condition in terms of our analytic parameters above. For a field atomic mass $A_f \simeq 1$ (protons), transition oscillator strength $f = 0.1$, and absorbing atomic charge $Z = 3$, the coulomb coupling condition is:

$$\frac{L_* v}{\dot{M}} < 5.9 \times 10^{16} , \tag{23}$$

in units of $L_\odot$, km s^{-1}, and $M_\odot$ yr^{-1} (Lamers & Cassinelli 1999).

3.4. *Line-driven Winds: Energy and Momentum*

Intuition for the energy transfer theory comes from Einstein's famous mass-energy equivalency equation, $E = Mc^2$. The rate of change of energy emitted from the star, i.e. it's luminosity, is then related to the rate of change of mass:

$$\frac{dE}{dt} = \frac{dM}{dt} c^2 \quad \rightarrow \quad L = \dot{M} c^2 . \tag{24}$$

Consider a hot luminous star with a stellar wind driven by a single line with rest frequency ν_0. Assume the wind has zero velocity at the photosphere ($r = 0$) and the velocity is terminal as r approaches infinity. Assume that the photosphere radially emits a continuum spectrum of photon frequencies and that the wind is very optically thick in the one line, such that photons with a frequency range from ν_0 to $\nu_0 (1 + v_\infty/c)$ are absorbed. The location of probable interaction for a photon with frequency in this range depends only the Doppler velocity of the wind. Photons with ν_0 can be absorbed immediately, and photons with $\nu_{\rm max} \equiv \nu_0 (1 + v_\infty/c)$ are absorbed at $r = \infty$. The total photospheric radiation absorbed per second is

$$L_{\rm abs} = \int_{\nu_0}^{\nu_{\rm max}} 4\pi R^2 \mathscr{F}_\nu \, d\nu , \tag{25}$$

and the momentum transferred is $L_{\rm abs}/c$ (Lamers & Cassinelli 1999). The outwards momentum of a wind with mass-loss rate $\dot{M}$ is $\dot{M} v_\infty$. In the single line model, outwards momentum of the wind must equal the momentum transferred to the wind such that

$$\dot{M} v_\infty = \frac{1}{c} \int_{\nu_0}^{\nu_{\rm max}} 4\pi R^2 \mathscr{F}_\nu \, d\nu \simeq \frac{4\pi R^2}{c} \mathscr{F}_{\nu_0} \nu_0 \frac{v_\infty}{c} , \tag{26}$$

where the last approximation can be made if the photospheric continuum spectrum is about constant over the frequency width. A key feature of this approximation is that it allows for an expression of mass-loss rate that is independent of the terminal velocity.

If the photosphere continuum spectrum is approximately a blackbody spectrum with effective temperature and frequency at the peak of the Planck law, (Equation22), then $\nu_{\rm max} \mathscr{F}_{\nu_{\rm max}} \simeq 0.62\ \sigma_B T_{\rm eff}^4$. Then, using the same relations earlier to rewrite flux at point r in terms of L_*, the mass-loss rate for a single, optically thick wind line is approximately

$$\dot{M} \simeq 0.62 L_*/c^2 \simeq L_*/c^2 .$$

Repeating the same approximation for a number $N_{\rm eff}$ optically thick lines, the mass-loss rate is:

$$\dot{M} \simeq N_{\rm eff} L_*/c^2 , \tag{27}$$

with the effective number of lines with large optical thickness given by,

$$N_{\rm eff} = \frac{\sum_{i=1}^{N} \int_{\nu_i}^{\nu_i (1+v_\infty/c)} \nu \mathscr{F}_\nu \, d\nu}{\int_0^\infty \mathscr{F}_\nu \, d\nu} .$$

Table 1. Observed properties of hot massive stars and their winds from Table 8.1 of Lamers & Cassinelli (1999). Ideally, $\eta_e = 0$ and $\dot{M}_{\rm pred} = \dot{M}$.

Parameter	ζ Pup	ϵ Ori	P Cyg	τ Sco	WR1
$L/L_\odot$	7.9×10^5	4.6×10^5	7.2×10^5	3.2×10^4	1.0×10^5
$T_{\rm eff}$ (K)	42400	28000	19300	30000	40000
$R/R_\odot$	17	33	76	6.5	2.2
$M/M_\odot$	59	42	30	15	9
$\dot{M}$ ($M_\odot$ yr^{-1})	2.4×10^{-6}	4.0×10^{-6}	1.5×10^{-5}	7.0×10^{-9}	6×10^{-5}
$N_{\rm eff}$	45	129	309	3.2	8800
v_∞ (km s^{-1})	2200	1500	210	2000	2000
η_e	2.2×10^{-4}	1.3×10^{-3}	1.1×10^{-3}	1.3×10^{-2}	1.0×10^{-2}
$\dot{M}_{\rm pred}$ ($M_\odot$ yr^{-1})	7.3×10^{-6}	6.2×10^{-6}	6.9×10^{-5}	3.2×10^{-7}	1.0×10^{-6}

Using this model, a star with $10^5 L_\odot$ would need $N_{\rm eff} = 150$ to achieve a mass-loss rate of $10^{-6} M_\odot {\rm yr}^{-1}$. As $N_{\rm eff}$ approaches infinity, the maximum mass-loss rate occurs when all of the emitted photons are absorbed and scattered:

$$\dot{M}_{\rm max} v_\infty = L/c\,. \tag{28}$$

This is known as the single-scattering limit for line-driven stellar winds.

Table 8.1 from Lamers & Cassinelli (1999) provides observational data for five "typical" early-type stars, a few relevant columns from their table is shown in Table 1 demonstrating the accuracy of the line driven theory, particularly taking into account the uncertainties in the derived values from observations. The accuracy score of the model using number of effective lines is given by $\eta_e = \left|\frac{N_{\rm eff} L}{\dot{M} c^2}\right| - 1$, (ideally zero), and the maximum predicted mass-loss rate is given by $\dot{M}_{\rm pred} = \frac{L}{c v_\infty}$.

3.5. *P Cygni Profiles*

In the outflow of stellar material, resonance lines of abundant ions with high oscillator strengths produce observable absorption lines. Since the winds are accelerated, a parcel of wind moving towards the observer has a velocity gradient, and the blue-shifted absorption lines can provide a measure of the wind velocity. Furthermore, if the wind parcel is moving quickly enough, the blue-shifted absorption line is "far away" enough and is resolvable from the central continuum emission profile observed in the stellar spectra. The central continuum is ejected in all directions, and the wind moving away from the observer produces red-shifted emission features. The combination of a single element's blue-shifted absorption and red-shifted emission lines is the eponymous *P Cygni profile*, named for the LBV hypergiant P Cygni, and shown in Figure 2. The mass column in shaded grey points from the star to the observer and contains the blue-shifted absorption lines with a maximum Doppler velocity corresponding to the terminal velocity of the wind. Continuum emission is emitted in all directions, but the component moving away from the observer contains red-shifted emission lines. The P Cygni profiles of the 3819.6 Å HeI and H_δ lines are shown in Figure 3.

4. COLLIDING WIND BINARIES

When two stars, both with strong outflows, are involved in a binary system, the wind interaction results in an immense and dynamic shock structure, whose temperature, instabilities and asymmetries manifest in a wide range of multi-wavelength phenomena. The high temperature shock-heated plasma produces X-rays via bremsstrahlung (free-free) emission, the ionized gas produces thermal radio emission and the accelerated, relativistic electrons produce synchrotron radiation in the radio, while dust grains formed in the denser, cooling gas also emit at infrared wavelengths (Lau et al. (2022); Tuthill et al. (1999), Williams et al. (1990)). The complex interplay of all these processes is not well understood, and continues to be pursued via observational and theoretical studies.

The stars in CWBs are characterized by extremely strong and dense stellar winds driven by radiation pressure on lines, as described above in Section 3. CWBs typically consist of WR or O type stars, with wind velocities on the order of $v_\infty \approx 1000 - 3000$ km s^{-1} and mass-loss rates around $\dot{M} \approx 10^{-5} - 10^{-4}$ $M_\odot$ yr^{-1}, and $\dot{M} \approx 10^{-7} - 10^{-6}$ $M_\odot$ yr^{-1},

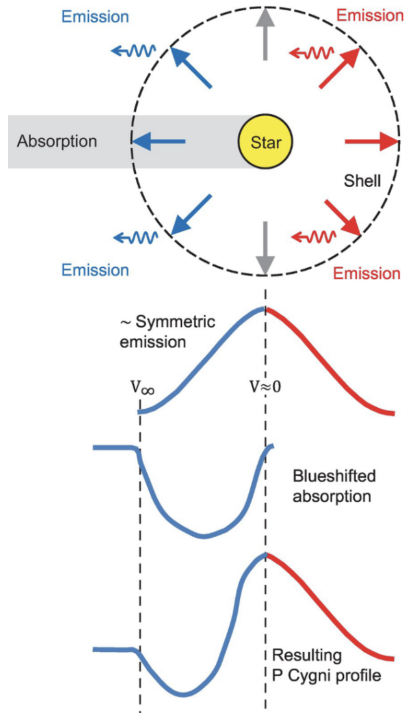

Figure 2. Schematic diagram of a P Cygni profile showing how blue-shifted and red-shifted absorption and emission contribute to the characteristic line shape. Image credit: Walker (2017).

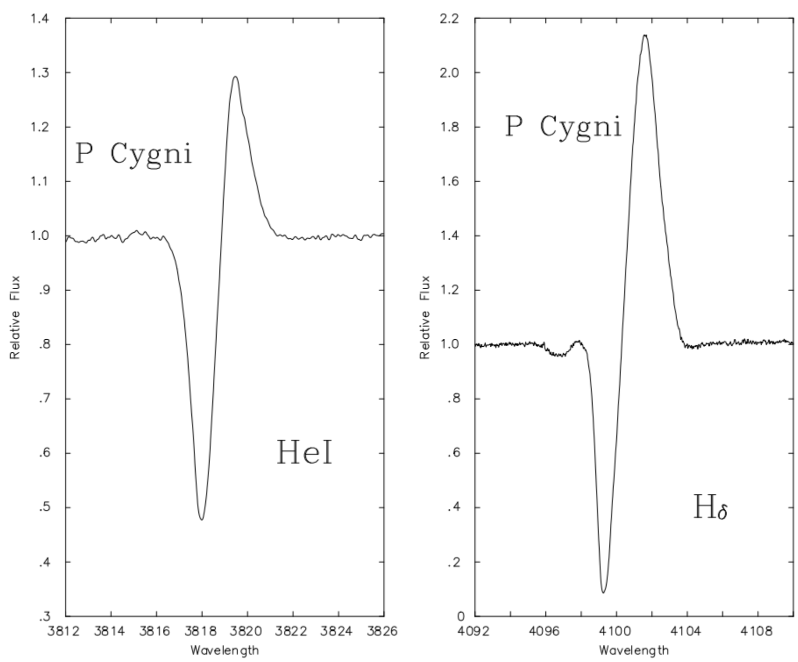

Figure 3. Observed HeI and H_δ lines from the LBV hypergiant P Cygni (Israelian & de Groot 1999).

respectively (Stevens et al. 1992). These extreme wind conditions lead to immense collisions between the stellar outflows, and the variety of orbital periods, eccentricities and differences in the strengths of the stellar outflows (their wind momenta) leads to a corresponding variation in the properties of emitting shock regions, e.g., their persistence, shape, size and luminosity. For example, the short period (220 ± 30 day), close ($1.9 - 2.6$ AU separation) and near

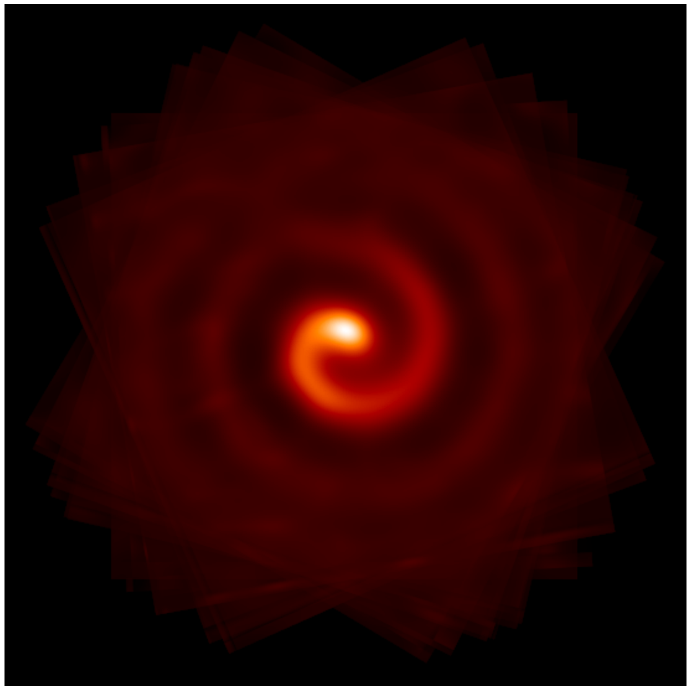

Figure 4. The archetypal "Pinwheel Nebula", WR 104, observed in the infrared (Tuthill et al. 1999).

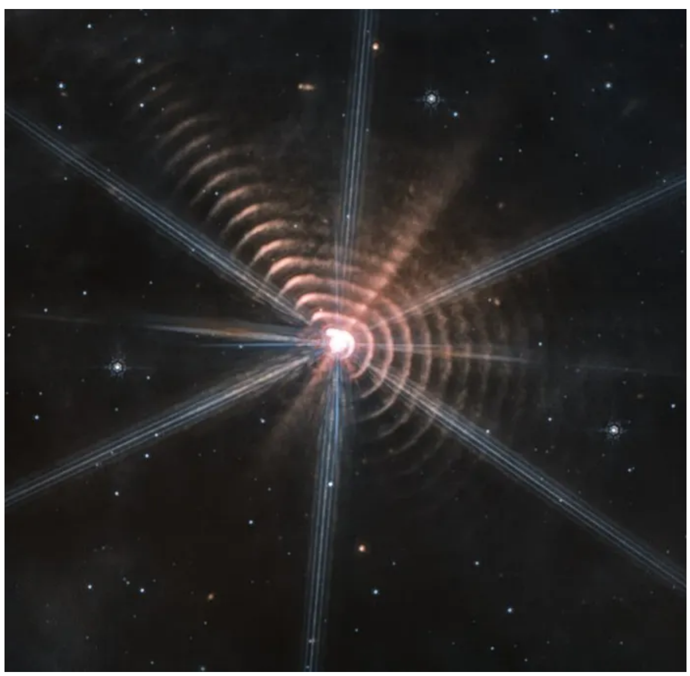

Figure 5. JWST MIRI image of the "nested dust shells" from the WR 140 colliding wind binary (Lau et al. 2022).

circular ($e < 0.06$) orbit of CWB WR 104 results in observed continuous dust formation, producing the archetypal *pinwheel nebula* shown in Figure 4 (Tuthill et al. 1999; Lamberts et al. 2012). On the other hand, the highly eccentric ($e = 0.89$) and long orbital period (2895 day) of CWB WR 140, (Figure 5), leads to periodic forceful wind collision, in which dust formation occurs only during periastron when the stars are separated by about 1.61 AU (Lau et al. 2022). Explaining the production of both X-rays and dust in the shocked regions is challenging. It is thought that the dense gas in the shock can cool rapidly and that a highly inhomogeneous, clumpy stellar wind might lead to dust formation where high density and opacity clumps shield delicate molecules and dust grains from the incident radiation fields, e.g., White & Tuthill (2024). The region of highly compressed, shocked wind between two massive stars is able to support and protect carbonaceous dust and carry them into the ISM.

4.1. *Wind Interaction Physics*

Obtaining predictable quantities from a CWB for comparison with observational data requires understanding of the physics of the wind interaction. The governing equations for the stellar outflows are the fluid continuity equation, as well as the conservation equations for momentum, thermal energy, and kinetic energy:

$$\frac{D\rho}{Dt} = 0, \quad \frac{D\boldsymbol{v}}{Dt} = -\frac{1}{\rho}\nabla P, \quad \frac{D}{Dt}(\rho\epsilon) = -P\nabla\cdot\boldsymbol{v}, \quad \frac{D}{Dt}\left(\frac{1}{2}\rho v^2\right) = -\mathbf{v}\cdot\nabla P\,, \tag{29}$$

where D/Dt is the material derivative, (defined in Equation 39), ϵ is the specific energy per unit mass, and we omit viscosity and gravity terms. In the steady-state, plane-parallel approximation, the material derivative reduces to a spatial derivative of one dimension since the system is symmetric in the other dimensions and is independent of time. The governing equations reduce to:

$$\frac{d}{dx}(\rho v) = 0, \quad v\frac{dv}{dv} = -\frac{1}{\rho}\frac{dP}{dv}, \quad \frac{d}{dx}(\rho\epsilon v) = -P\frac{dv}{dx}, \quad \frac{d}{dx}\left(\frac{1}{2}\rho v^2\right) = -v\frac{dP}{dx}\,. \tag{30}$$

The first of these neatly leads to the conclusion that $\rho v = \text{const}$. Performing chain rule differentiation and substituting into the reduced momentum conservation equation leads to $\rho v^2 + P = \text{const}$. Finally, adding together the thermal and kinetic energy conservation statements and substituting yields $\frac{1}{2}v^2 + \epsilon + P/\rho = \text{const}$. These conditions are assigned '1' and '2' subscripts denoting the pre-shock and post-shock values, and are known as the *Rankine-Hugonoit* jump conditions:

$$\rho_1 v_1 = \rho_2 v_2\,, \tag{31}$$

$$\rho_1 v_1^2 + P_1 = \rho_2 v_2^2 + P_2\,, \tag{32}$$

$$\frac{1}{2}v_1^2 + \epsilon_1 + \frac{P_1}{\rho_1} = \frac{1}{2}v_2^2 + \epsilon_2 + \frac{P_2}{\rho_2}\,. \tag{33}$$

These equations are typically written in terms of the *Mach number*, $\mathcal{M} \equiv v/c_s = \sqrt{\frac{\rho v^2}{\gamma P}}$, where c_s is the sound speed. A "strong shock" occurs when the fluid speed is much larger than the speed of sound, $\mathcal{M} \gg 1$. The adiabatic Rankine-Hugonoit conditions can be rewritten in terms of the mach number, and once the strong shock condition is applied, reduce to the following:

$$\frac{\rho_2}{\rho_1} = 4, \quad v_2 = \frac{1}{4}v_1, \quad T_2 = \frac{3}{16}\frac{\mu m_H}{k_B}v_1^2\,. \tag{34}$$

For an isothermal equation of state, (isothermal is defined as $T_1 = T_2$), the strong shock conditions are:

$$\frac{\rho_2}{\rho_1} = \frac{v_1^2}{c_s^2}, \quad v_2 = \frac{c_s^2}{v_1}\,, \tag{35}$$

where the sound speed of the gas is

$$c_s = \sqrt{\frac{k_B T}{\mu m_H}}\,. \tag{36}$$

For two sufficiently strong winds colliding with each other, the surface of the interaction will form a planar *contact discontinuity*. If both winds have reached their terminal velocity, they experience little acceleration and the pressure terms of the second Rankine-Hugonoit condition (Equation 32) drop out. Then, writing the wind density in terms of velocity using mass continuity (Equation 5) yields the distances from each star to the plane (d_1 and d_2) in terms of their wind terminal velocities and mass-loss rates (Stevens et al. 1992):

$$\left(\frac{\dot{M}_1 v_1}{\dot{M}_2 v_2}\right)^{1/2} = \frac{d_1}{d_2}\,. \tag{37}$$

The theoretical location of the contact discontinuity provides a metric to test simulation data. Figure 6 depicts a schematic diagram of the contact discontinuity formed by the stellar wind collision of two stars.

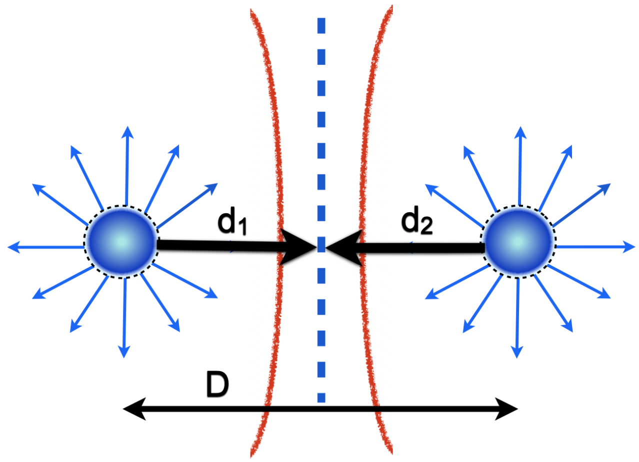

Figure 6. Schematic diagram of the wind collision region showing the position of the contact discontinuity (dashed line) in a colliding wind binary. Image credit: S. Mohamed.

4.2. *Radiative Cooling and Shock Instabilities*

The specific hydrodynamics of the compressed, shocked gas is complicated by radiative cooling. Specifically, radiative cooling alters the energy conservation equations described in Section 4.1, and even more importantly, results in hydrodynamic instabilities in the wind collision regions. While we included isothermal models rather than taking into account detailed radiative cooling in this paper, we give a brief summary of how radiative cooling affects the shocks in CWBs more broadly. The cooling and heating processes in the shock-compressed region of CWBs include line cooling, dust heating and emission, inverse Compton cooling, photo-ionization and free-free emission. In their discussion of radiative cooling in CWBs, Stevens et al. (1992) introduce a cooling time parameter, given by the ratio of the time it takes the shocked gas to radiate its thermal energy ($t_{\rm cool}$) and the time it takes the shocked gas to flow out of the shock region ($t_{\rm esc}$):

$$\chi \equiv \frac{t_{\rm cool}}{t_{\rm esc}} \approx \frac{v_8^4 d_{12}}{\dot{M}_{-7}} \tag{38}$$

where v_8 is the wind velocity in units of 1000 km s^{-1}, d_{12} is the distance to the contact discontinuity in units of 10^7 km $= 10^{12}$ cm, and $\dot{M}_{-7}$ is the mass-loss rate of the star in units 10^{-7} $M_\odot$ yr^{-1}, where the cooling rate is approximated as constant for the ranges of wind temperatures typically in CWBs (Stevens et al. 1992). The cooling parameter χ characterizes the importance of radiative cooling: for $\chi \gtrsim 1$ the wind is adiabatic, while for $\chi \ll 1$ the wind is isothermal. Furthermore, since Equation 38 shows that $\chi \propto d$, it follows that the cooling parameter characterizes the orbital period: $\chi \propto P^{3/2}$. Use of this simple model demonstrates that CWBs with larger periods are expected to be more adiabatic. Stevens et al. (1992) also indicate that χ is more important to the system if the wind collision shocks occur at oblique angles.

Possibly even more importantly, Stevens et al. (1992) show that structural dynamic instabilities grow rapidly as the cooling parameter χ increases. The thermal instability of the shocked gas is related to the cooling rate, and Kelvin-Helmholtz instabilities arise due to velocity shear along the discontinuity. Regardless, the evolution of CWBs can certainly be characterized by the stability or instability of substructures formed in the shocked material, the nature of which can be studied using high resolution multi-dimensional hydrodynamic simulations.

5. THE AREPO CODE

We use the AREPO code (Springel 2010). The behavior of a set of particles is uniquely determined by solving a corresponding set of differential equations. Given a set of initial conditions, numerical simulations uniquely provide predictions for the behavior of a system by performing numerical integrations for the governing differential equations and updating the positions of each particle in a time-step evolution. As computing power and sophisticated software continue to advance, numerical simulations become more and more accurate at predicting a system's time evolution. AREPO is one such code which generates predictions of the evolution of systems through use of a moving-mesh magnetohydrodynamics (MHD) algorithm. While AREPO has been widely used for large-scale cosmological simulations and galaxy formation and morphology, (Nelson et al. 2021), it has also been used for smaller-scale, isolated systems, like the common envelope phase of binary stars (Ohlmann et al. 2016). Here, AREPO is used to test the theoretical understanding of stellar wind models and the shocks in CWBs.

5.1. *Discretization*

The challenge of numerical simulations is accurately representing real world, continuous systems in discrete space and time. The solution does not lie in simply implementing a grid on which to obtain discrete space and perform calculations, as this leads to further problems: How do you set up a grid to represent highly non-uniform fluids? How do you efficiently parallelize computing when one cell may have many more calculations to perform than another? Some methods like SPH, (smoothed particle hydrodynamics), (Gingold & Monaghan 1977; Lucy 1977), employ a Lagrangian fluid specification in which the code frame automatically follows fluid parcels through use of the *material* or *convective* derivative (Zingale 2025):

$$\frac{D}{Dt} \equiv \frac{\delta}{\delta t} + \boldsymbol{u} \cdot \nabla \,. \tag{39}$$

These methods have the benefit of tracking the position, velocity and acceleration as functions of time at the location of the particle, and leads to high understanding of a fluid's advection (Zingale 2025).

On the other hand, Eulerian methods concern a fixed, finite volume region and track particles as they enter and exit this fixed frame. Simulation codes with Eulerian grids can partition the grid to higher resolution depending on the density of the fluid and calculate the flux through each partitioned cell's boundaries to obtain a larger picture of the fluid. By measuring how the fluid's hydrodynamic properties change over time at a fixed location, this methodology is particularly useful for laminar flows and systems with known fixed boundaries (Robertson et al. 2010). However, each method has its limitations. Eulerian methods provide no history of individual particles, and Lagrangian methods are difficult to accommodate boundary conditions and can be computationally expensive.

The AREPO code is a quasi-static Euler-Lagrangian moving-mesh code which combines the advantages of both methods. AREPO operates on a dynamic, moving Voronoi mesh. The mesh is constructed via Voronoi Tessellation in which cells are generated around a mesh-generating point, and whose boundaries define the region of space in which all points are closest to a single mesh-generating point (Weinberger et al. 2020). The boundaries between Voronoi cells are inherently equidistant between mesh-generating points, and are perpendicular to the line connecting any two points (Figure 7). The set of Voronoi cell boundaries forming lines equidistant to mesh-generating points form three-dimensional tetrahedra, known as a Delaunay triangulation. The circumsphere of each Delaunay tetrahedron will always contain a single mesh-generating point (Weinberger et al. 2020), providing an extremely useful and insightful means of discretizing space to compute hydrodynamic equations and evolve time steps. The combination of the Voronoi Tessellation and the Delaunay topological dual-space counterpart results in a unique and most optimal triangulation of any set of two dimensional points (Springel 2010). Furthermore, the adaptive mesh refinement (AMR) scheme employed by AREPO automatically refines or de-refines cells based on physical quantities in the cells. For the hydrodynamic simulations presented here, the refinement criterion is a "reference gas particle mass", which varied from simulation to simulation and acts as a resolution parameter, e.g., dividing cells into smaller and smaller elements at the regions of interest, such as the high-density shock interface.

5.2. *Finite Volume Hydrodynamics*

The governing differential equations for compressible, inviscid fluids are the Euler equations for conservation of mass, momentum, and energy. Springel (2010) introduces a state vector and flux equation

$$\boldsymbol{U} = \begin{pmatrix} \rho \\ \rho \boldsymbol{v} \\ \rho u + \frac{1}{2}\rho \boldsymbol{v}^2 \end{pmatrix} , \tag{40}$$

$$\boldsymbol{F}(\boldsymbol{U}) = \begin{pmatrix} \rho \boldsymbol{v} \\ \rho \boldsymbol{v}\boldsymbol{v}^{\boldsymbol{T}} + P \\ (\rho\epsilon + P)\boldsymbol{v} \end{pmatrix} , \tag{41}$$

with equation of state, $P = (\gamma - 1)\rho\epsilon$, in order to compactly express the Euler equations as:

$$\frac{\partial \boldsymbol{U}}{\partial t} + \boldsymbol{\nabla} \cdot \boldsymbol{F} = 0 \,. \tag{42}$$

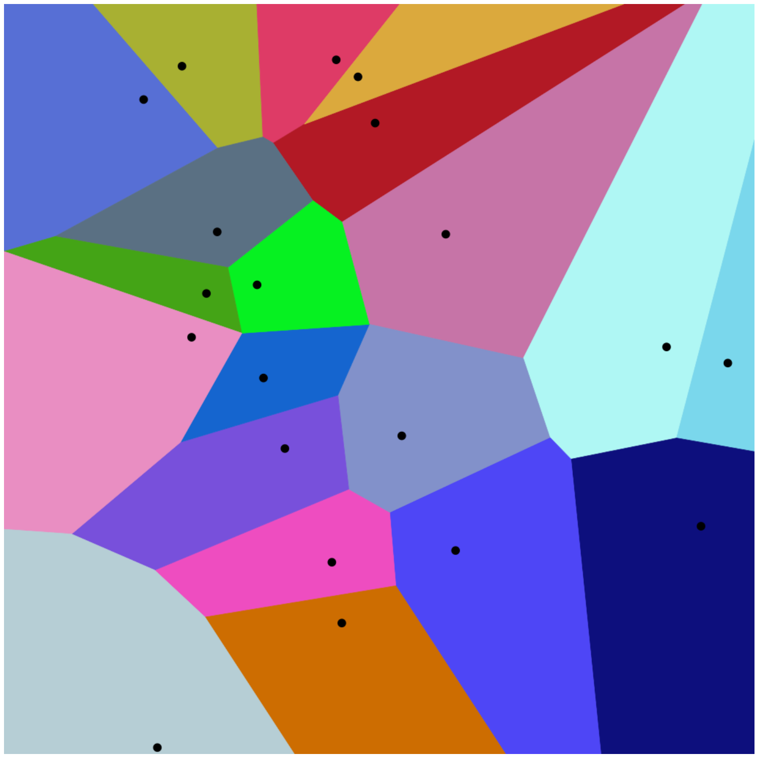

Figure 7. 2D example of a Voronoi tessellation. The cells are colored so that space in each cell is closest to a single point. Note how the cell boundaries form lines equidistant to points on either side, and that lines connecting any two points are always normal to the cell boundary. Image credit: by Balu Ertl.

To compute conserved quantities for each cell, Springel (2010) adopts a *finite-volume* approach, in which the computational domain is subdivided into a finite number of cells, whose averages are used to calculate conserved quantities. This translates to an integral over the volume of each cell to define the mass, momentum and energy of each cell:

$$\boldsymbol{Q}_i = \begin{pmatrix} m_i \\ \boldsymbol{p}_i \\ E_i \end{pmatrix} = \int_{V_i} \boldsymbol{U} dV \, . \tag{43}$$

Use of the *Divergence Theorem* and the compact Euler equations (Equation 42) leads to a surface flux integral around the surface of each cell. Since in 3D the cells are polyhedra with flat polygonal faces, Springel (2010) define $\boldsymbol{A}_{ij}$ as the vector area between any two cells i and j, such that the averaged flux across the boundary is

$$\boldsymbol{F}_{ij} = \frac{1}{A_{ij}} \int_{A_{ij}} \left(\boldsymbol{F}(\boldsymbol{U}) - \boldsymbol{U}\boldsymbol{w}^{\boldsymbol{T}} \right) d\boldsymbol{A}_{ij} \, , \tag{44}$$

where $\boldsymbol{w}$ is the velocity of the cell boundary points ($\boldsymbol{w} \neq \boldsymbol{v}$ exactly, see Springel (2010) section 3). The finite volume form of the Euler equations is then:

$$\frac{d\boldsymbol{Q}_i}{dt} = -\sum_j A_{ij} \boldsymbol{F}_{ij} \, . \tag{45}$$

5.3. *Time Integration*

The global time discretization between flux time integrations is a modified Courant–Friedrichs–Lewy (CFL) condition

$$\Delta t_i = C_{\rm CFL} \frac{R_i}{c_i + |\boldsymbol{v}_i - \boldsymbol{w}_i|} \, , \tag{46}$$

where $\boldsymbol{v}$ and $\boldsymbol{w}$ are the fluid and cell boundary velocities, respectively, R is the cell radius as a function of cell volume $R = (3V/\pi)^{1/3}$, (or $R = (V/\pi)^{1/2}$ in 2D), $c_i = \sqrt{\gamma P/\rho}$ is the speed of sound in the cell, and $C_{\rm CFL} \approx 0.4 - 0.8$ is

Table 2. Code units of stellar wind simulations and relevant physical constants. Constants μ and γ represent the mean molecular weight and the adiabatic index, respectively.

Name	Value
UNITMASS	1 $M_\odot$
UNITLENGTH	1 $R_\odot$
UNITVELOCITY	10^8 cm s^{-1}
UNITTIME	696 s
UNITDENSITY	5.90 g cm^{-3}
UNITENERGY	1.99×10^{49} erg
UNITSPECINT	10^{16} erg g^{-1}
m_H	1.67×10^{-24} g
k_B	1.38×10^{-16} erg K^{-1}
μ	1.2
γ	5/3

the CFL coefficient. In the hydrodynamic simulations presented here, adaptive time-stepping is used where the initial global timestep of the simulation is determined, and then individual cell timesteps are calculated taking into account the minimum CFL timestep of all the cells, plus additional constraints from source physics.

5.4. *Temperature Issues at Low Resolutions*

Galilean invariance is a classical mechanical principle which states that laws of motion are the same in all reference frames. In the context of computational hydrodynamics, in order for a fluid to be Galilean-invariant, the physical conserved quantities of the fluid must appear the same from all observer reference frames. This poses a difficult problem for hydrodynamic simulations. AREPO, the moving-mesh solution presented by Springel (2010), is a Galilean-invariant code. However, AREPO still struggles with issues of "spurious dissipation" leading to incorrect temperature calculations. This arises when there is poor resolution in areas where the fluid flow is much larger than the speed of sound. In the case of stellar winds in CWBs, the high wind velocities leads to supersonic fluids, which leads to poor temperature calculations for these kinetically dominated flows in the case of insufficient resolution. Due to finite time and computational resources, the 3D simulations presented in Section 6 suffer from compounding discretization errors which leads to too high simulated temperatures. One possible solution, which we plan to explore in future work, is to evolve the entropy rather than energy in these regions.

6. SIMULATIONS AND ANALYSIS

We present simulations of single and binary stellar winds with a variety of different system parameters and resolutions. The simulation code units and relevant constants are given in Table 2. While the hydrodynamic evolution is computed by AREPO, initial conditions (ICs) are required to set up the problem, with the relevant stellar and domain boundaries, as well as the initial parameters and stellar wind properties to evolve. To accomplish this, we use the Python HEALPix (Hierarchical Equal Area isoLatitude Pixelation) package, *healpy*, to set up discretized spherical shells as stellar boundaries. The role of the ICs is to ensure that the boundaries of the stars are well defined, to ensure that the stellar boundaries continuously eject wind material at densities, velocities and temperatures required, and to mark these cells so that the code does not evolve, deform, or (de)refine them. The number of boundary cells, and their corresponding IDs or "types" are carefully set, determining resolution in the IC shells. The computational methods used to ensure successful setup of the ICs were then redesigned to accommodate 2D simulations.

6.1. *Three-Dimensional Initial Conditions*

The initial simulation variable parameters are the wind velocity and temperature, stellar masses, radii, and mass-loss rates. The resolution of the healpix shells is determined by a resolution parameter set at the start of each simulation, N. The initial number of mesh-generating Voronoi points is equal to $N_{\rm BDRY} = 12 \times N^2$. Through use of the Python package *healpy*, we set up four concentric spherical shells, each with $N_{\rm BDRY}$ points, separated radially by a small spacing parameter, d. The outermost shell simulates boundary of the star. The particles are ejected through the outermost "sticky" boundary, which is a no-slip boundary in which the boundary particles are forced to be immobile. Across the no-slip "sticky" boundary, the fluid has zero relative velocity with respect to the boundary. The fluid also has zero tangential flow at the boundary. The inner shells consist of either "solidside" or "fluidside" boundaries, which are reflective boundaries. For the reflective boundaries, the normal component of the fluid velocity is reversed, while the parallel components are preserved. Physical hydrodynamic quantities are copied over across the boundary at each time step such that the reflective boundaries act like a mask over the region representing the star. The IC shells are placed over a background grid, with resolution parameter $N_{\rm BDRY} = N_{\rm CPD}^3$ evenly-spaced background mesh points, in a cube of length $L_{\rm box}$. The volume of the ISM is $L_{\rm box}^3$, and the total mass of the ISM is determined by the volume and the density, which is a variable simulation parameter. The initial specific internal energy of the ISM is a function of the initial ISM temperature, which is a simulation variable:

$$U(T) = \frac{k_B T}{\mu m_H (\gamma - 1)} \,. \tag{47}$$

The initial ejection specific internal energy of the wind is computed by the same equation. The initial wind parameters are then concatenated into spherical arrays and compiled into an hdf5 file using the Python package *h5py*. For binary star stellar wind systems, the stellar boundaries are duplicated and their centers are placed equidistant from the grid's center.

6.2. *Two Dimensional ICs*

The governing physical equation for stellar wind, the continuity equation, has a different form in two dimensions:

$$\dot{M} = 2\pi R \rho(r) v(r) \,. \tag{48}$$

The simulation variable parameters in 2D are mostly the same as those in the 3D case, except rather than a healpix resolution parameter N, the resolution of the now *circular* shells is set by the spacing parameter of the shells, d, via:

$$N_\phi = \frac{20\pi R}{d} + 1 \,, \tag{49}$$

where R is the radius of the star. Rather than setting up spherical arrays with *h5py*, we manually set the circular boundary points using the x and y coordinates of the stellar centers, and placing points in a circle around each stellar center using angle

$$\alpha_i = \frac{2\pi(i + 0.5)}{N_\phi} \,. \tag{50}$$

6.3. *Single Star Tests*

To learn how to properly operate, understand, and interpret results from AREPO, we begin by simulating the hydrodynamic outflows of a single stellar wind. We construct radial histograms of the simulated density, temperature and velocity, and overlay the three physical quantities with analytical results from Equations 11 and 14. We used a standard Runge-Kutta algorithm to perform numerical integration of Equation 11. We were unable to achieve a convergent numerical solution for the velocity differential equation (Equation 12). This may be due to mistakes in the derivation of the differential equation or errors in implementing the numerical integration. Either way, since the simulated stellar winds have such incredibly high velocities, we assume no wind deceleration or acceleration towards the center of the star, leading to a predicted constant velocity result. We ran many test simulations to understand the impact of different input and resolution parameters. The four single stellar wind simulations presented are named 3DLow, 3DHigh, 2DLow, and 2DHigh, where "high" or "low" refers to the relative resolution of the simulations. Simulation variable input parameters for the four single star runs are shown in Table 3.

We encountered issues with the radial profiles where even at high resolution the velocity and temperature profiles did not line up with the predicted analytical solution. We suspect that this is due to the shape of first cells surrounding the stellar boundaries in the initial conditions. If the first binned simulation density does not occur at the exact same radial coordinate as the ejected density in the initial condition file, then there will be a scaling error due to the ejected density either occurring too far or too close to the center. In our case, we found that in 3D was a slight

Table 3. Parameters for the 2D and 3D low and high resolution, single stellar outflow simulations, in code units, with the exception of mass-loss rate ($\dot{M}$) which is in the standard units of solar masses per year ($M_\odot$/yr). N is the healpix resolution parameter discussed in Section 6.1, d is the shell spacing parameter, and RGPM is the reference gas particle mass, which is the criterion for refinement based on cell mass. Here, Δt simply refers to the amount of simulation time between snapshots, and does not refer to the integration time of the simulation.

	3DLow	3DHigh	2DLow	2DHigh
R	10	10	3	3
v_0	3	3	1.22	1.22
T_0	20000	20000	45000	45000
ρ_0 or σ_0	5.85×10^{-14}	5.85×10^{-14}	2.88×10^{-11}	2.88×10^{-11}
$\dot{M}$ [$M_\odot$/yr]	10^{-5}	10^{-5}	3×10^{-5}	3×10^{-5}
N	16	64		
N_ϕ			377	377
d	0.5	0.2	0.2	0.2
RGPM	10^{-16}	10^{-16}	10^{-13}	10^{-15}
$N_{\rm CPD}$	32	64	128	128

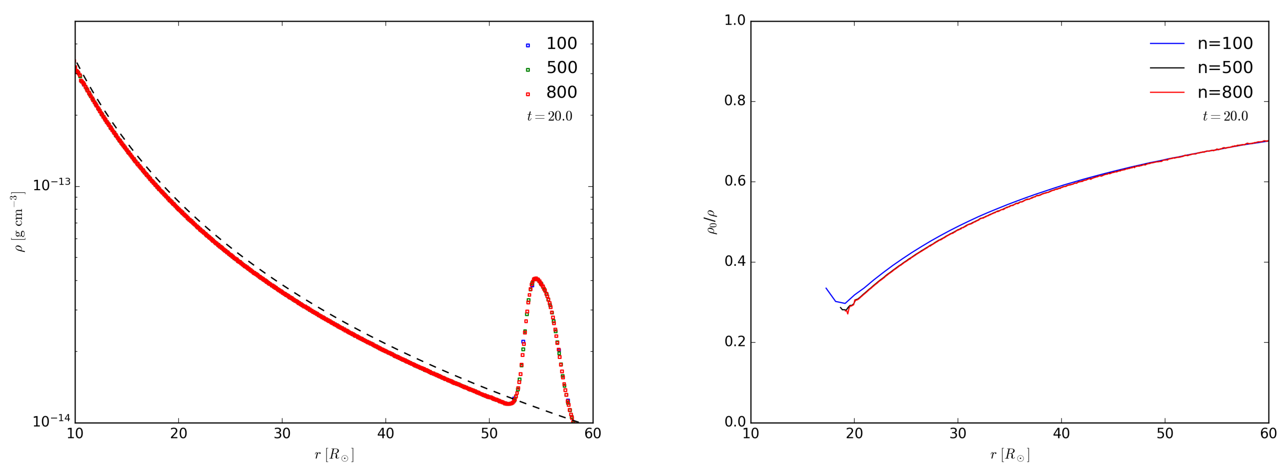

Figure 8. Comparison of the 3DHigh density radial profiles while varying bin resolution. Left: three different bin resolutions in comparison to the analytical solution (black dashed line). Right: analytical density divided by simulation density (ρ_0/ρ) for the same bin resolution comparison.

under-density, even at high resolution. To ensure that the observed simulation under-density was not due to binning resolution (number of bins when constructing radial profiles), we run a test on the 3DHigh run where we construct the radial profiles at 100, 500, and 800 bins, and demonstrate the multiplying factor between the simulation and analytical densities (Figure 8).

Figure 8 confirms that the observed under-density is not due to poor bin resolution. To fix the under-density, we identify the calculated density in the first bin of the simulation radial profile, and scale the analytical solution so that the initial densities align. The bin-scaling corrected radial profiles for the 3DLow and 3DHigh runs are shown in Figure 9. We show that the predicted constant velocity wind matches the simulated result. However, the 3DLow result achieves only an approximately accurate density result, and a very poor temperature result, while the higher resolution 3DHigh result is able to achieve highly accurate density profiles. The poor temperature result in the higher-resolution 3D run is due to the concerns discussed in Section 5.4. We were unable to achieve high enough resolution in the 3D runs to achieve accurate temperature calculation given our limited computational resources and time. Figure

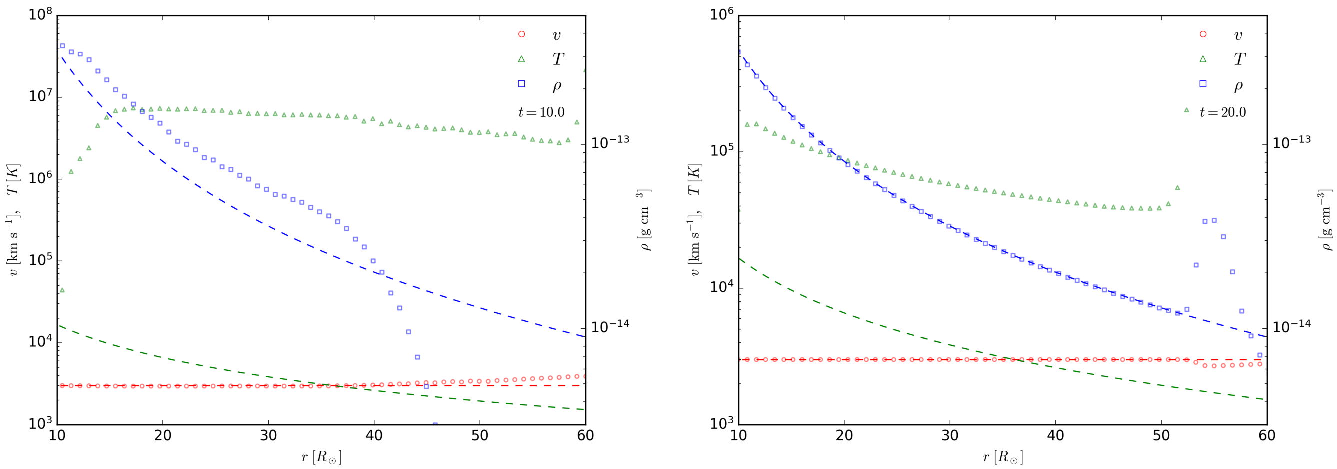

Figure 9. Radial profile snapshots at t=10.0 for the 3DLow (left) and 3DHigh (right) simulation runs. Temperature and velocity data are plotted on the left axis of each plot, and density is plotted on the right axis of each plot.

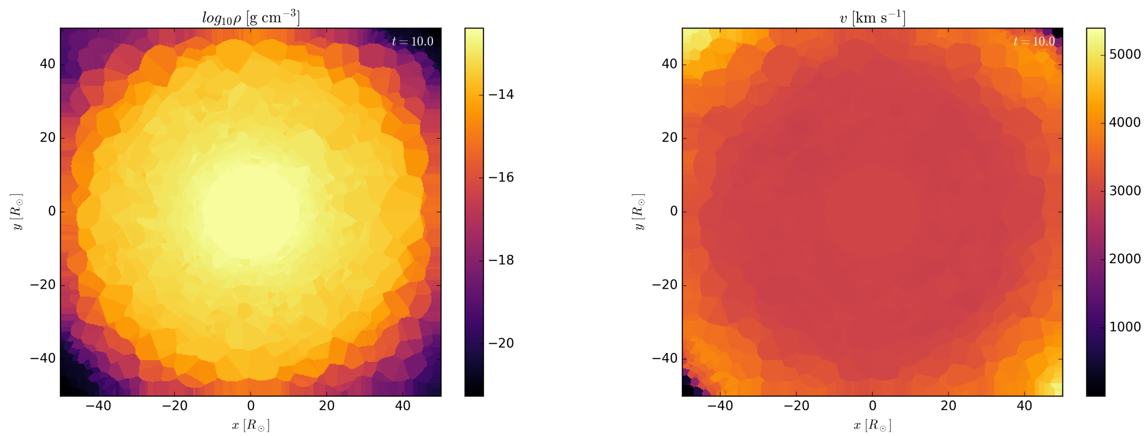

Figure 10. 3DLow density and velocity cross sections.

10 and 11 show late snapshots of the 3DHigh and 3DLow cross sections for the simulation density, temperature and velocity. The 3DLow temperature cross section results were omitted since they neither match the shape nor scale of the analytical solution. On the other hand, the 3DHigh temperature cross section results were included since the shape approximately matches the analytical solution, while only the scale is incorrect. The 3DHigh temperature cross section computed values are incorrect, but the morphology of the temperature gradient matches the analytical solution for a single spherically symmetric stellar wind. The cross section plots for all three hydrodynamic quantities display the shockwave produced by the initial wind ejection colliding with the ISM. Since we are not modeling shock physics for the single star case, the shock wave should be disregarded and only material inside the shock should be considered. It is also notable from the velocity cross sections and radial profiles that the simulation does an excellent job of maintaining constant velocity inside the relevant region (within the shock).

To achieve sufficient resolution given our time and computational constraints, we opted to carry out further tests and the binary simulations in 2D, allowing for higher resolution and saving computational power and time. Since the governing equations supporting the derivation of the density and velocity differential equations discussed earlier are inherently three dimensional, we opt to use solely the 2D continuity equation (Equation 48) as our analytical solution for the 2D simulations. We are able to demonstrate that the Runge-Kutta numerical integration of the density differential equation is equivalent to the 3D continuity equation for a symmetric stellar outflow (see Figure 12). Then, since the 2D continuity equation is the exact reduced-dimensionality analog of the 3D continuity equation, the

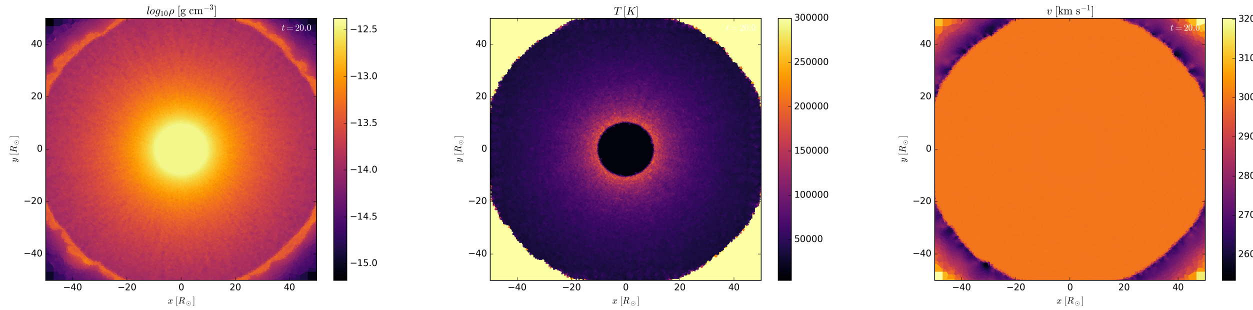

Figure 11. 3DHigh density, temperature and velocity cross sections.

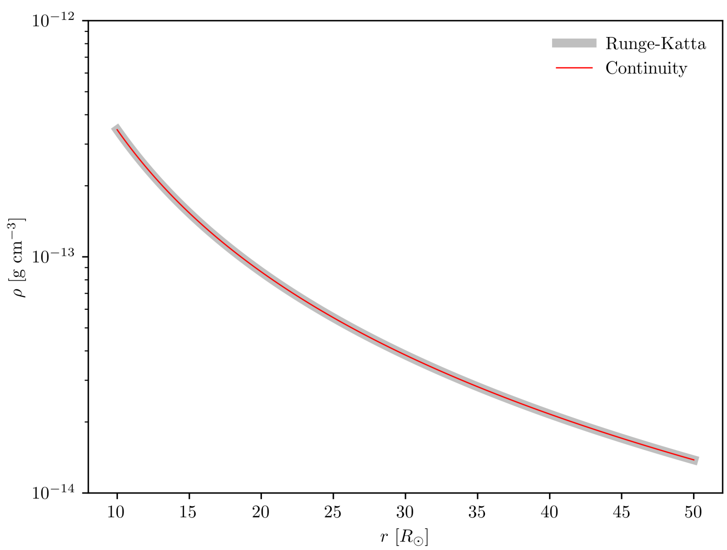

Figure 12. Runge-Kutta numerical integration of the density differential equation (Equation 11) along with the analytical solution from the 3D continuity equation for constant velocity, both as a function of radius.

2D continuity equation is an accurate representation of an analytical solution to circular symmetric stellar outflows. The same temperature analytical solution is used for testing the 2D simulations, and the velocity is, again, assumed to be constant.

Radial histograms of the 2D simulations were constructed and compared to the analytical results discussed above, similar to the 3D runs. The combined radial profile of the 2DLow and 2DHigh runs is shown in Figure 13, while late snapshot cross sections of the 2DLow and 2DHigh densities, temperatures and velocities are shown in Figures 14 and 15. The 2D radial profiles were bin-scaled again, scaling the analytical solution to the first calculated simulation quantity. Note that even with the bin scaling and higher resolution of the 2DLow simulation there is still a slight inaccuracy in simulated temperature. This, again, is likely due to poor resolution, since we demonstrate that good temperature agreement is finally achieved in the 2DHigh run. There was user error in setting up the 2DLow simulation which caused the boundaries of the simulation to not act as inflow-outflow boundaries, resulting in material reflecting off the boundary and forming non-physical instabilities with the outflow, thus the edge instabilities should be ignored; the inner region of the cross section accurately matches the analytical solution.

The agreement of the 2D profiles with the analytical solution in correspondence with the accuracy between the Runge-Kutta and continuity equations and the physical analog of the 2D to the 3D continuity equations leads us to believe that the initial conditions setup and subsequent evolution in AREPO result in the expected properties and evolution of a steady state, spherically symmetric stellar outflow. The analysis and results of these single star tests

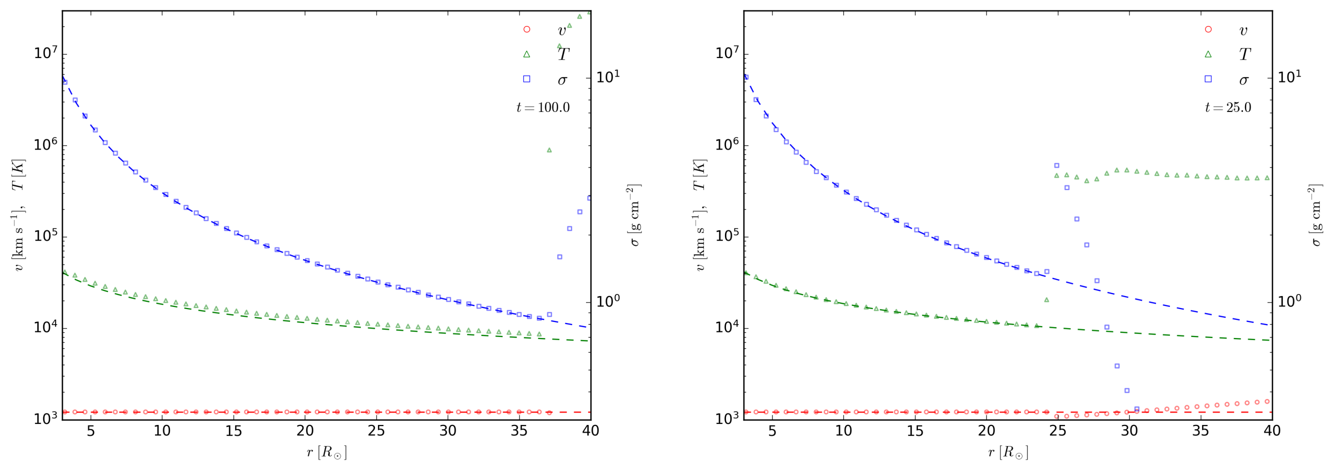

Figure 13. Latest time combined radial profile snapshot for the 2DLow (left) and 2DHigh (right) simulation runs. Temperature and velocity data are plotted on the left axis of each plot, and density is plotted on the right axis of each plot.

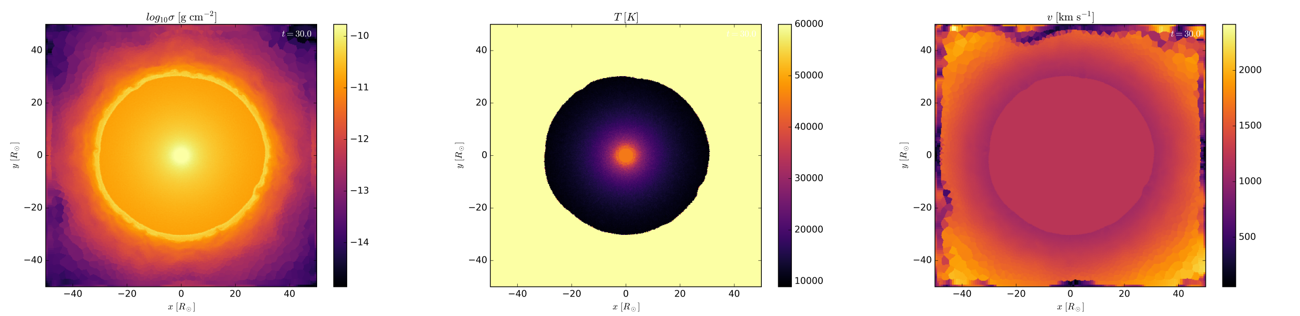

Figure 14. 2DLow density, temperature and velocity cross sections. Ignore instabilities at box edges.

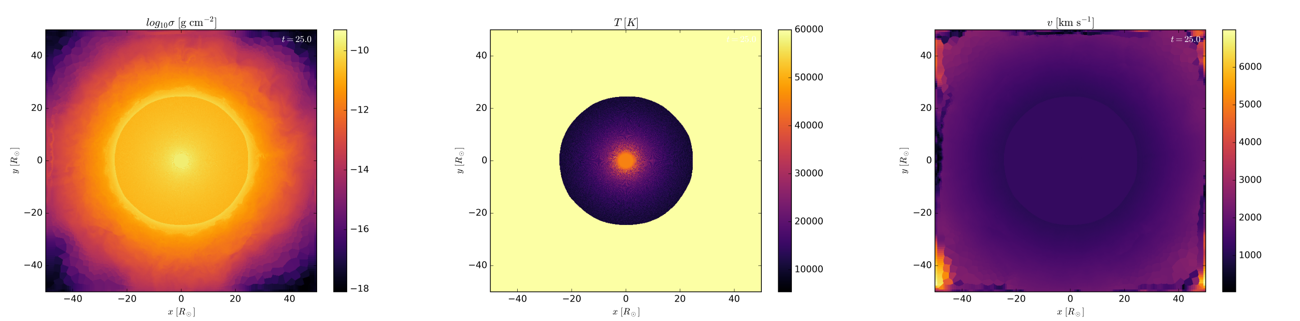

Figure 15. 2DHigh density, temperature and velocity cross sections.

improved our understanding of the numerical setup and solvers in AREPO and was also useful for developing and testing the necessary simulation interpretation and analysis scripts and tools.

6.4. *Simulating Colliding Wind Binaries*

Due to limited time and computational resources, all CWB simulations were performed in two dimensions. [1] The above single stellar outflow models were necessary to test the setup and results in AREPO for a simplified case where

[1] The rendered plots below show the structures that would form in the binary orbital plane, we thus refer to them as 'cross sections'.

Table 4. Simulation parameters for the four CWB models. Since each simulation is for a pair of stars, each table entry with a comma-separated pair indicates the values for each star, while entries with a single value indicates the value is the same for both stars. Each simulation is also assigned a run nickname, allowing for easy reference. Both stars for all four runs have $M_1 = M_2 = 10\ \mathrm{M}_\odot$, $R_1 = R_2 = 3\ \mathrm{R}_\odot$, $T_1 = T_2 = 45000$ K, and semi-major axis $a = 0.3$ AU $= 64.7\ \mathrm{R}_\odot$. The time between each snapshot for all runs is $\Delta t = 0.5$. Units are in code units unless otherwise specified.

	Equal	Corotate	Isothermal	Unequal
$\dot{M}_1$, $\dot{M}_2$ [$\mathrm{M}_\odot$ yr^{-1}]	3×10^{-5}	3×10^{-5}	3×10^{-5}	3×10^{-5}, 3×10^{-6}
$v_{0,1}$, $v_{0,2}$	1.22	1.22	1.22	1.22, 2
RGPM	10^{-12}	10^{-12}	10^{-12}	10^{-13}
N_{snap}	611	414	446	611

exact analytical solutions can be derived. The CWB simulations presented here are again idealized with the goal of comparing the results to analytical estimates and expectations. These CWB simulations, therefore, act as a stepping stone towards understanding the intricate and complex hydrodynamics of a colliding wind region, bolstered by our confidence in the ability of the AREPO code to accurately capture the physics of the stellar outflows and shocks. The simulation parameters for the four main CWB simulations are shown in Table 4. We present two stationary binaries, "Equal" and "Unequal", along with two binaries in the co-rotating frame of reference, "Corotate" and "Isothermal". The stationary binary simulations are applicable in the case that the wind velocity is much greater than the orbital velocities of the member stars, which is likely in wide systems when the CWB consists of one or more WR stars. Of the stationary binaries, the first, "Equal", features two stars with equal wind velocities and mass-loss rates, resulting in the ideal shock interaction structure discussed at length by Stevens et al. (1992). The second stationary binary, "Unequal", is a higher resolution simulation of two stars with unequal mass-loss rates but the same wind velocity. The other two CWB simulations account for the orbital motion of the two stars through space by enabling the simulation particles to be accelerated via the Coriolis and centrifugal forces. Therefore, both the "Corotate" and "Isothermal" runs are simulated in the co-rotating frame of the CWB, while the "Isothermal" run uses an isothermal equation of state in addition. The isothermal sound speed is $c_s = 0.0167$, from Equation 36. Both co-rotating simulations have equal mass-loss rates and wind velocities.

6.4.1. *Analysis of CWB cross sections and radial profiles*

Density and velocity cross sections for the "Isothermal" CWB are shown in Figure 16, in which the winds of both stars are subject to strong cooling, leading to expected thin-shell instabilities in the contact discontinuity. The isothermal equation of state results in the width of the shock being much smaller than in the adiabatic case. Density, velocity and cross section plots for the equal stationary "Equal" CWB are shown in Figure 17. In the wind collision, kinetic energy is converted to thermal energy, heating the gas which expands outwards away from the contact discontinuity. As was found in previous studies, the latter is subject to strong instabilities (e.g., the Kelvin-Helmholtz instability produced by shear between the two stellar winds). The density plot (top left) exhibits the classic contact discontinuity modeled extensively by Stevens et al. (1992) and resembles their model. Figure 18 demonstrates the adiabatic co-rotating frame with Coriolis and centrifugal forces. Here, the width of the shock is much larger than in the isothermal case. Figure 19 demonstrates the unequal stationary binary, resulting in the "bow-shock-like" outflow from the stronger star towards the weaker. Figure 20 is a line profile plot of the density for the latest evolution of the "Unequal" CWB. Applying the mass-loss rates and velocities to equation 37 yields a prediction for the location of the contact discontinuity. Equation 37 predicts $d_1/d_2 = 2.47$. Based on the density line profile shown in Figure 20, we estimate a contact discontinuity location of 13.45 $\mathrm{R}_\odot$ to the right of the center. Since each star is spaced 32.34 $\mathrm{R}_\odot$ from center, the simulated ratio of each star's distance to the contact discontinuity is 2.42. Our "Unequal" CWB simulation is able to achieve the predicted value from Equation 37 to within 1.9% of the predicted result.

In the non-isothermal cases, the temperature of the gas in the shocked region is so much larger than the gas in the non-shocked regions that the non-shocked regions appear to have temperature towards zero. We see that the

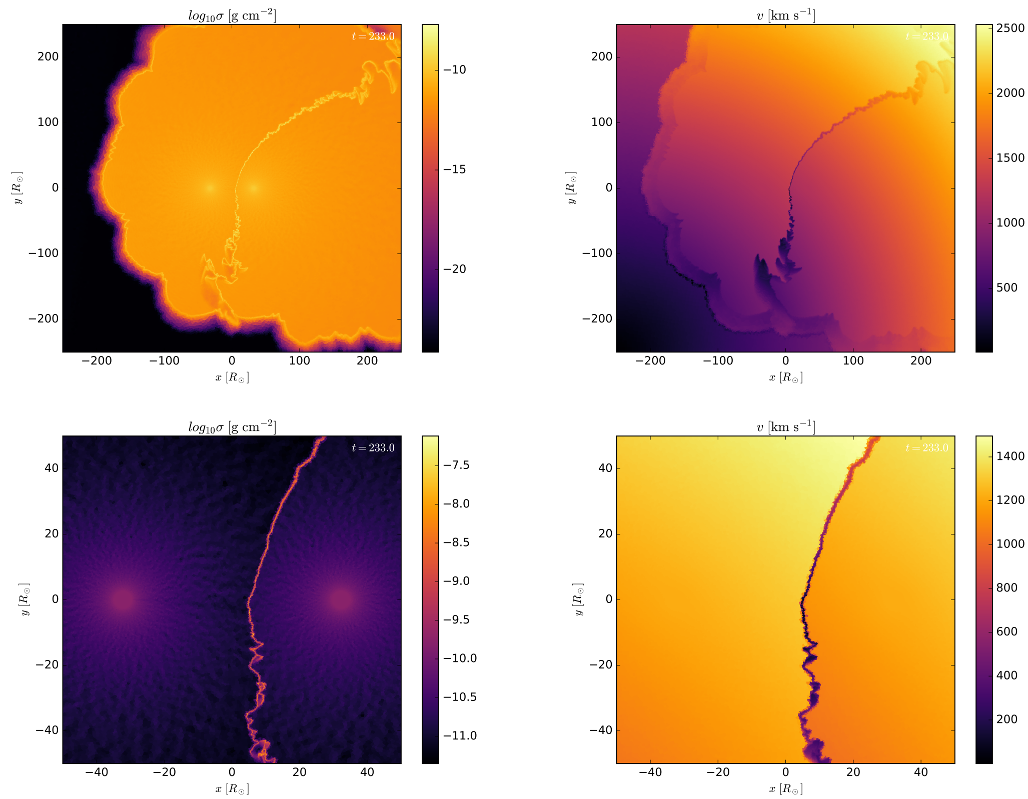

Figure 16. Cross section plots of the isothermal co-rotating frame CWB. Left: Full view of density simulation (top) and zoom of closest approach contact discontinuity (bottom). Right: Full view of velocity simulation (top) and zoom of closest approach contact discontinuity (bottom).

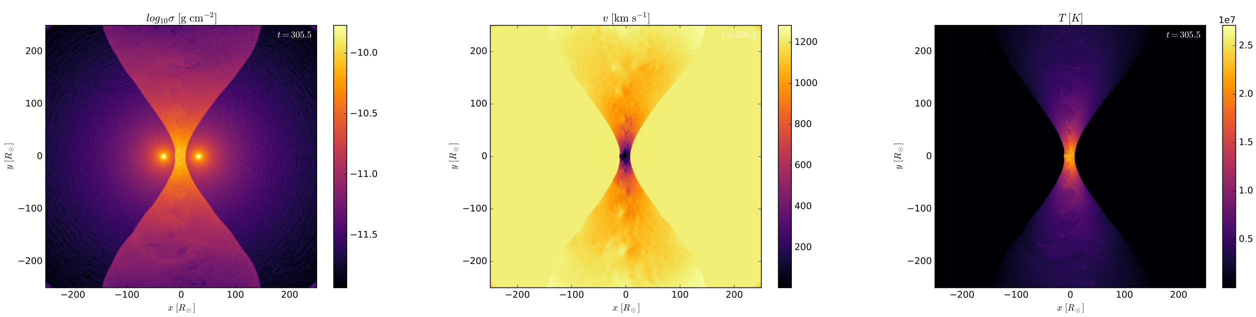

Figure 17. Cross section plots of Equal CWB.

temperature is highest in the areas of maximal gas compression, and that this intuitively corresponds with the smallest gas velocities.

In addition to the full simulation "Isothermal" run, which was in the co-rotating frame, we ran a partial simulation of a "stationary" isothermal CWB in order to test the isothermal jump conditions discussed in Section 4.1. Figure 21 shows the density cross sections and line profiles for similarly evolved isothermal (Left) and adiabatic (Right) strong shocks. We estimate the initial ρ_1 density by drawing a line through the lowest density region immediately before the shock. Since the shocked region contains a wide range of densities, we draw a line through the region that approximates the average density of the highest number density of plotted points. Based on the estimated lines drawn for the isothermal line profile, we approximate $\rho_1 = 2.3 \times 10^{-12}$ [g cm^{-2}] and $\rho_2 = 1.5 \times 10^{-8}$ [g cm^{-2}], leading to $\rho_2/\rho_1 \approx 6521$. The analytical solution for an isothermal strong shock states that $\rho_2/\rho_1 = v_1^2/c_s^2 = 5337$, using our

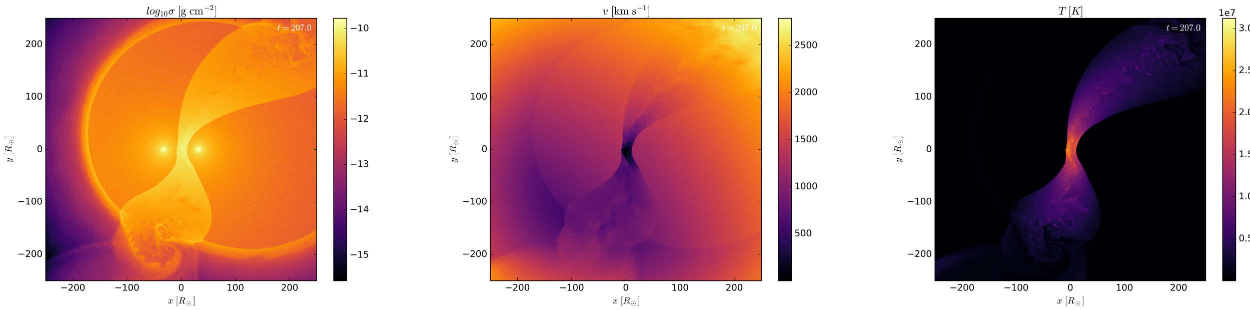

Figure 18. Cross section plots of the Corotating, adiabatic CWB.

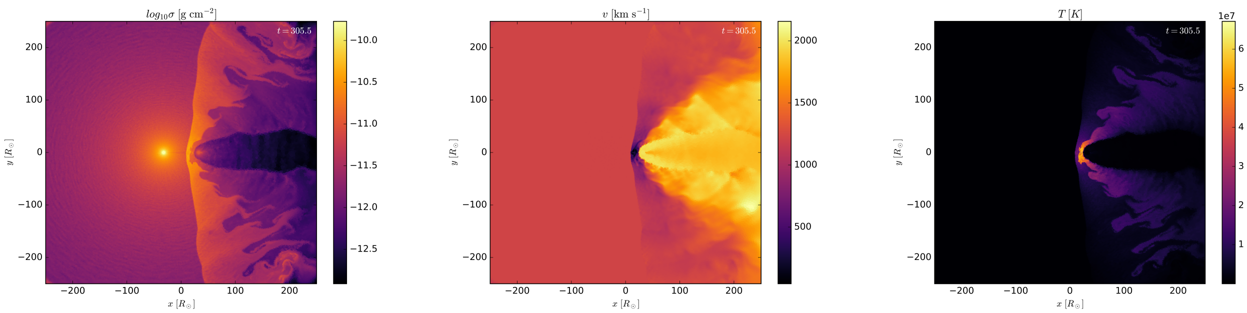

Figure 19. Cross section plots of the stationary Unequal CWB.

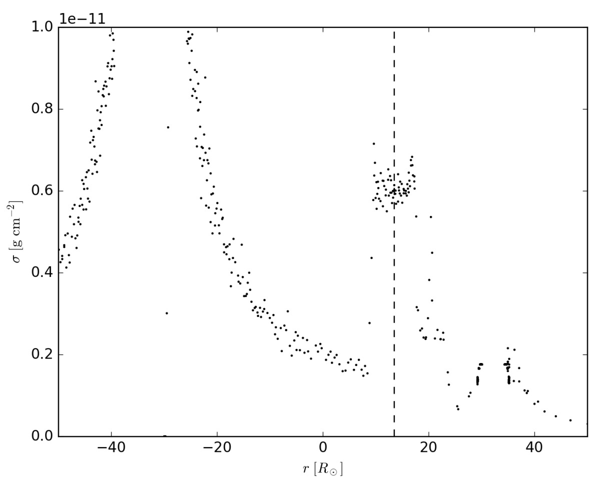

Figure 20. Density line profile of the latest snapshot of the Unequal CWB.

value of $c_s = 0.0167$ for the isothermal speed of sound and $v_1 = 1.22$. Our value is accurate to within 22%, which is reasonable due to the uncertainties in determining the pre-shock values for highly unstable gas and the low simulation resolution. Since we simulate a wide field around the CWB, we expect the shock resolution to be low. Since the isothermal shocks are even smaller, the analytical values will suffer even more from poor shock resolution. From the density line profile of the similarly-evolved adiabatic shock, (Figure 21-Right), we estimate $\rho_1 = 0.6 \times 10^{-12}$ [g cm^{-2}] and $\rho_2 = 2.45 \times 10^{-12}$ [g cm^{-2}], leading to $\rho_2/\rho_1 \approx 4.08$, which is within 2% of the theoretical value of $\rho_2/\rho_1 = 4$, from Equation 34.

Figure 22 shows the temperature cross section and line profile from the same adiabatic strong shock as Figure 21. The initial temperature is $T_1 = 45000$ K. From the line profile, we estimate that the shocked temperature is

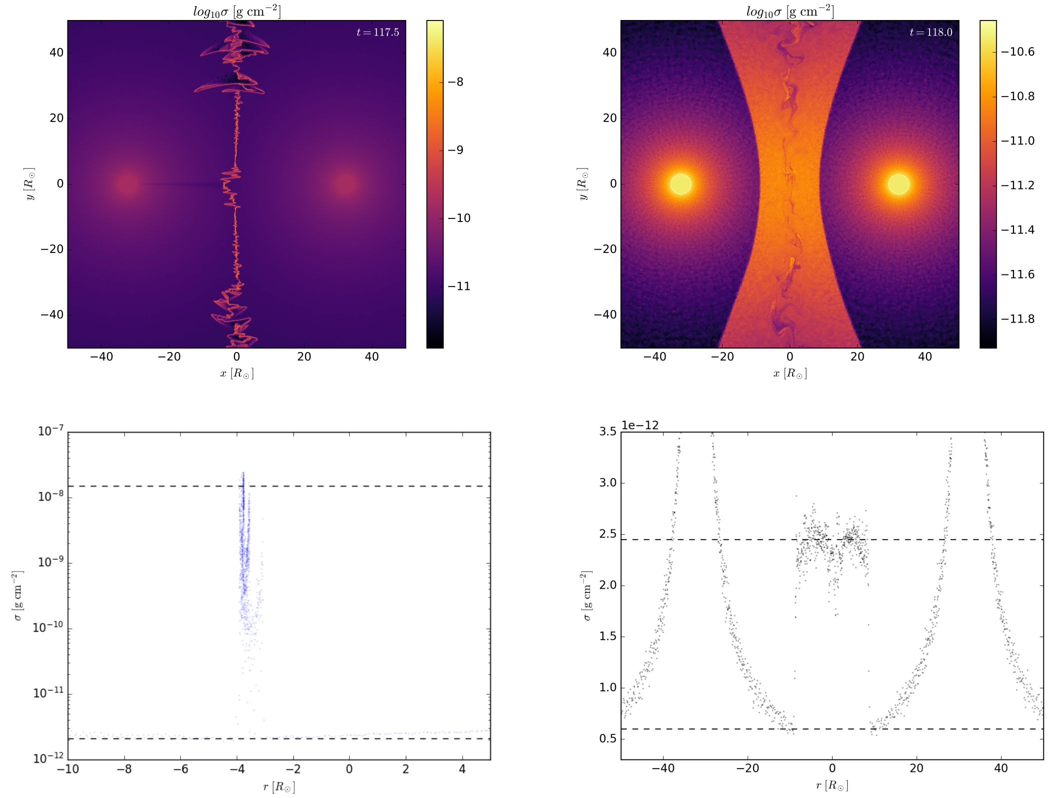

Figure 21. Line profile analysis for similar timesteps of a stationary adiabatic (right column) and isothermal (left column) strong shock.

$T_2 \approx 2.2 \times 10^7$ K. From Equation 34, the analytical shocked temperature is $T_2 = 2.03 \times 10^7$ K. Our simulated shocked temperature is accurate to within 8.6%.

Figure 23 demonstrates the same time evolution of the velocity cross sections and line profiles of the adiabatic (Right) and isothermal (Left) shocks. The isothermal analytical result for shocked velocity is $v_2 = c_s^2/v_1$, so, since the sound speed is low, the expectation is that $v_2 \ll 1$. From the velocity line profile, we estimate a shocked velocity of $v_2 \approx 0.03$. From the sound speed and wind velocity, the expected isothermal shocked wind velocity is 2.3×10^{-4}. Our result velocity is still too high for the analytical solution, but it matches the expectation that $v_2 \ll 1$. A more accurate shocked velocity value would be obtained from a higher shock resolution, which is amplified, again, by the thin isothermal shock. From the adiabatic velocity line profile, we estimate $v_2 \approx 0.2$, which, when compared to the initial wind velocity of $v_1 = 1.22$, results in $v_2/v_1 \approx 0.16$, which is accurate to the analytical result of 0.25 to within 34%. The adiabatic shocked velocity is much more accurate than the isothermal shock velocity since the larger size of the shock leads to a higher shock resolution.

7. CONCLUSIONS AND FURTHER WORK

Through a series of 2D and 3D simulations, we have shown that AREPO can capture the basic physics required to represent the outflow from a single, spherically (or circularly) symmetric star. We were also able to simulate in 2D colliding wind binaries, accurately predicting the location and stability of the contact discontinuity, as well as replicating the strongly-shock values expected for density, velocity and temperature for both isothermal and adiabatic shocks. Our simulations were limited by finite physical and computational time, and we would be able to achieve higher accuracy and precision results with more resources and the incorporation of additional physics. For example, to improve the temperatures derived in the simulations in poorly resolved flows, we could evolve the gas entropy rather than than the energy. Additionally, we could include more detailed physics for radiative cooling, account for stellar rotation and with more computational resources, or simulate CWBs in 3D, since the shock instabilities are expected to behave differently in higher dimensions van Marle & Keppens (2012).

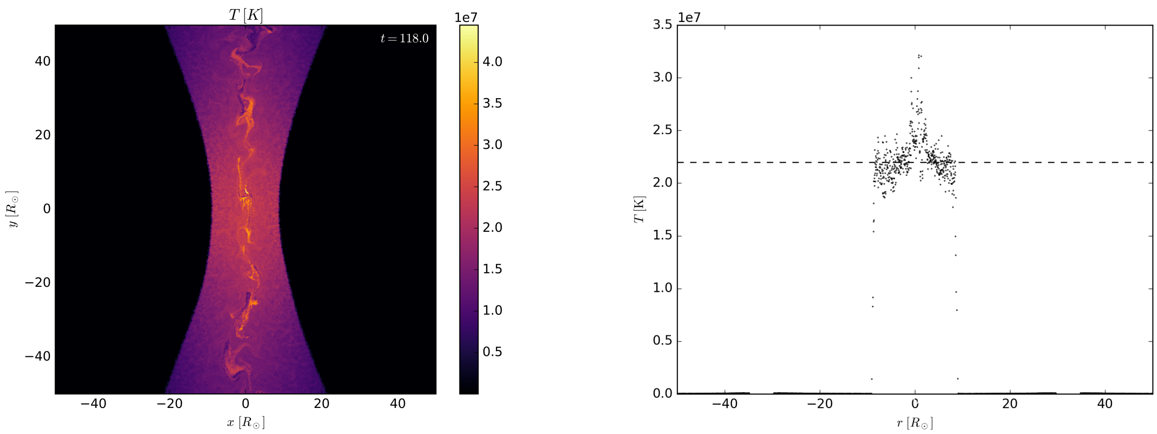

Figure 22. Temperature cross section and line profile for the adiabatic strong shock.

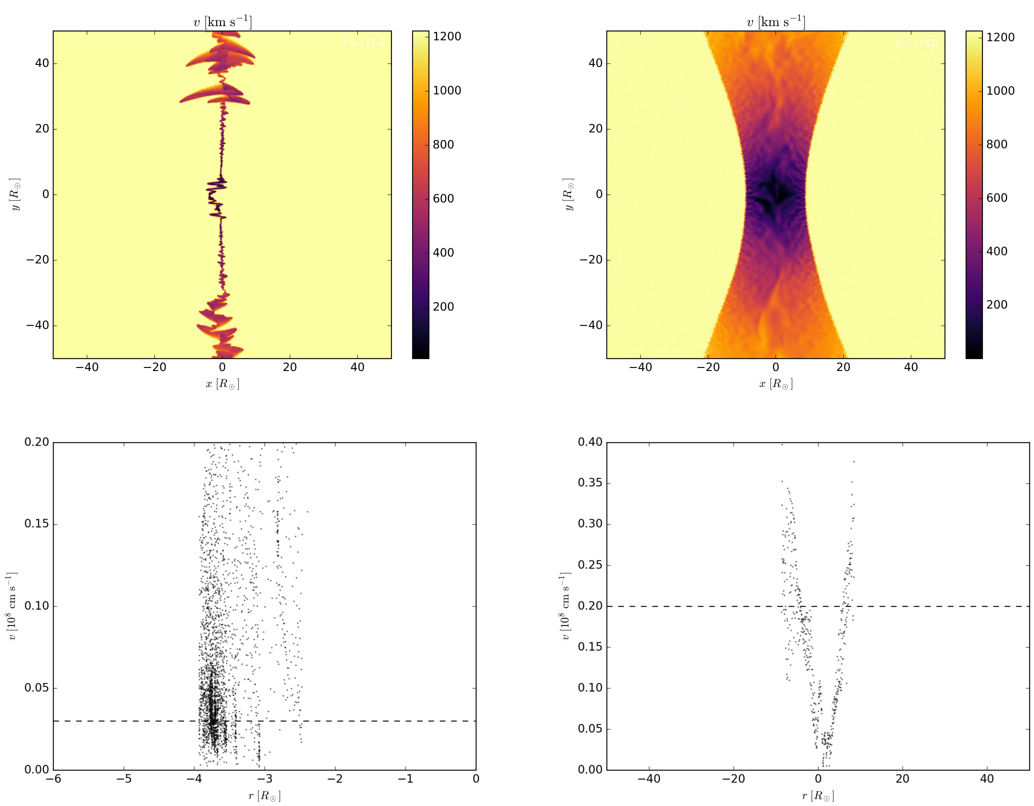

Figure 23. Velocity cross sections and line profiles for adiabatic (right column) and isothermal (left column) strong shocks.

AREPO is an inherently magnetohydrodynamic code, therefore in addition to exploring a wider range of parameters like wind momenta and orbital properties, further work on this project might incorporate the effects of magnetic fields on stellar winds and wind interactions. Combining this with relevant physical processes like dust formation, free-free and synchrotron emission, these models could serve as a basis for generating observables from the simulated CWBs to make predictions for comparison and interpretation of radio, infrared and X-ray observations. This would allow us to advance our understanding of these systems, and could serve as a set of initial conditions for further modeling of supernovae interactions with complex cirumstellar media, advancing our understanding of late stage stellar evolution.

REFERENCES

Abbott, D. C., & Conti, P. S. 1987, ARA&A, 25, 113, doi: 10.1146/annurev.aa.25.090187.000553

Brott, I., de Mink, S. E., Cantiello, M., et al. 2011, A&A, 530, A115, doi: 10.1051/0004-6361/201016113

Cassinelli, J. P. 1979, ARA&A, 17, 275, doi: 10.1146/annurev.aa.17.090179.001423

Chandrasekhar, S. 1939, An introduction to the study of stellar structure (University of Chicago Press)

Clapeyron, B. P. É. 1834, Mémoire Sur la Puissance Motrice de la Chaleur (Journal de l'École Polytechnique)

Crowther, P. A. 2007, Annual Review of Astronomy and Astrophysics, 45, 177–219, doi: 10.1146/annurev.astro.45.051806.110615

de Jager, C., Nieuwenhuijzen, H., & van der Hucht, K. A. 1988, A&AS, 72, 259

Edgar, R. 2004, NewAR, 48, 843, doi: 10.1016/j.newar.2004.06.001

Gawryszczak, A. J., Mikołajewska, J., & Różyczka, M. 2002, A&A, 385, 205, doi: 10.1051/0004-6361:20011800

Gingold, R. A., & Monaghan, J. J. 1977, Monthly Notices of the Royal Astronomical Society, 181, 375, doi: 10.1093/mnras/181.3.375

Israelian, G., & de Groot, M. 1999, SSRv, 90, 493, doi: 10.1023/A:1005223314464

Lamberts, A., Dubus, G., Lesur, G., & Fromang, S. 2012, Astronomy & Astrophysics, 546, A60, doi: 10.1051/0004-6361/201219006

Lamers, H. J. G. L. M., & Cassinelli, J. P. 1999, Introduction to Stellar Winds (Cambridge University Press)

Lau, R. M., Hankins, M. J., Han, Y., et al. 2022, Nature Astronomy, 6, 1308–1316, doi: 10.1038/s41550-022-01812-x

Lucy, L. B. 1977, AJ, 82, 1013, doi: 10.1086/112164

Nelson, D., Springel, V., Pillepich, A., et al. 2021, The IllustrisTNG Simulations: Public Data Release. https://arxiv.org/abs/1812.05609

Ohlmann, S. T., Röpke, F. K., Pakmor, R., & Springel, V. 2016, ApJL, 816, L9, doi: 10.3847/2041-8205/816/1/L9

Panagia, N., & Bono, G. 2000, Pre-Supernova Evolution of Massive Stars. https://arxiv.org/abs/astro-ph/0003201

Pols, O. 2011, Stellar Structure and Evolution, Astronomical Institute Utrecht

Robertson, B. E., Kravtsov, A. V., Gnedin, N. Y., Abel, T., & Rudd, D. H. 2010, Monthly Notices of the Royal Astronomical Society, 401, 2463, doi: 10.1111/j.1365-2966.2009.15823.x

Rybicki, G. B., & Lightman, A. P. 1985, Radiative Processes in Astrophysics (New York, NY: Wiley), doi: 10.1002/9783527618170

Sana, H., de Mink, S. E., de Koter, A., et al. 2012, Science, 337, 444, doi: 10.1126/science.1223344

Smith, L. F. 1968, MNRAS, 138, 109, doi: 10.1093/mnras/138.1.109

Smith, N. 2017, Interacting Supernovae: Types IIn and Ibn, ed. A. W. Alsabti & P. Murdin (Cham: Springer International Publishing), 403–429, doi: 10.1007/978-3-319-21846-5_38

Spitzer, L. 1962, Physics of Fully Ionized Gases (Interscience Publishers)

Springel, V. 2010, Monthly Notices of the Royal Astronomical Society, 401, 791–851, doi: 10.1111/j.1365-2966.2009.15715.x

Stevens, I. R., Blondin, J. M., & Pollock, A. M. T. 1992, ApJ, 386, 265, doi: 10.1086/171013

Tuthill, P. G., Monnier, J. D., & Danchi, W. C. 1999, Nature, 398, 487–489, doi: 10.1038/19033

van der Hucht, K. A. 2001, VizieR Online Data Catalog: 7th Catalog of Galactic Wolf-Rayet stars (van der Hucht, 2001), VizieR On-line Data Catalog: III/215. Originally published in: 2001NewAR..45..135V

van Marle, A. J., & Keppens, R. 2012, A&A, 547, A3, doi: 10.1051/0004-6361/201218957

Walker, R. 2017, Spectral Atlas for Amateur Astronomers: A Guide to the Spectra of Astronomical Objects and Terrestrial Light Sources (Cambridge University Press)

Weinberger, R., Springel, V., & Pakmor, R. 2020, The Astrophysical Journal Supplement Series, 248, 32, doi: 10.3847/1538-4365/ab908c

White, R. M. T., & Tuthill, P. 2024, arXiv e-prints, arXiv:2412.12534, doi: 10.48550/arXiv.2412.12534

Williams, P. M., van der Hucht, K. A., Pollock, A. M. T., et al. 1990, MNRAS, 243, 662

Zingale, M. 2025, Introduction to Computational Astrophysical Hydrodynamics (Open Astrophysics Bookshelf)